On the validity of the uniform thermodynamic state approach for underground caverns during fast and slow cycling

Murad S. Abuaisha, Ahmed Rouabhi

▶ **To cite this version:**

Murad S. Abuaisha, Ahmed Rouabhi. On the validity of the uniform thermodynamic state approach for underground caverns during fast and slow cycling. International Journal of Heat and Mass Transfer, 2019, 142, pp.118424. 10.1016/j.ijheatmasstransfer.2019.07.074 . hal-02197140

HAL Id: hal-02197140
https://hal.science/hal-02197140

Submitted on 25 Oct 2021

HAL is a multi-disciplinary open access archive for the deposit and dissemination of scientific research documents, whether they are published or not. The documents may come from teaching and research institutions in France or abroad, or from public or private research centers.

L'archive ouverte pluridisciplinaire **HAL**, est destinée au dépôt et à la diffusion de documents scientifiques de niveau recherche, publiés ou non, émanant des établissements d'enseignement et de recherche français ou étrangers, des laboratoires publics ou privés.

Distributed under a Creative Commons Attribution - NonCommercial 4.0 International License

Version of Record: https://www.sciencedirect.com/science/article/pii/S0017931019306507
Manuscript_c43d33b101295f33f98794224e8db14f

On the validity of the uniform thermodynamic state approach for underground caverns during fast and slow cycling

Murad AbuAisha[a,*], Ahmed Rouabhi[a]

[a]*MINES ParisTech, PSL Research University, Centre de Géosciences, 35 rue Saint Honoré, 77300, Fontainebleau, France*

Abstract

Gas storage in underground caverns provides a promising technique to reply efficiently to the renewable energy needs through periods of intermittency. An appropriate prediction of the cavern performance, in terms of thermal inventory and the quantity of stored or retrieved gas, depends on the gas thermodynamics and the thermo–mechanical response of the surrounding rock.

The rate of injected or withdrawn mass to/from caverns controls the spatial heterogeneities of the temperature and pressure fields. It also controls the magnitude of gas velocity which represents the driving force for the convective heat transfer with the surrounding rock domain. In order to consider as many industrial concerns during cycling as possible (for instance rock creep and gas diffusion), researchers tend to simplify the cavern thermodynamic problem by neglecting the spatial variations of pressure and temperature which leads to a cavern uniform state. This reduces tremendously the simulation cost, yet it raises up a question about the validity of such assumption during fast cycling. We will be addressing this concern by performing simplified (uniform thermodynamic state) and complete simulations that take into account all the complexities of this computational fluid dynamics problem. A discussion section at the end of this paper will provide us with a margin of trust with regard to the simplified approaches for seasonal and daily cycling of underground caverns.

Keywords: Underground caverns; fast and slow cycling; uniform thermodynamic state; spatial heterogeneities; finite element simulations

1. Introduction

The intermittency problem that usually characterizes renewable energy led to vast storage techniques in the last few decades [1–4]. Hydrogen/energy storage in solution–mined caverns [5, 6] is one of the suggested solutions. In this context, a precise prediction of the cavern thermodynamic state is needed.

*Corresponding author
Email addresses: murad.abuaisha@mines-paristech.fr (Murad AbuAisha), ahmed.rouabhi@mines-paristech.fr (Ahmed Rouabhi)

© 2019 published by Elsevier. This manuscript is made available under the CC BY NC user license
https://creativecommons.org/licenses/by-nc/4.0/

Besides, such a thermodynamic response requires to be fully coupled with the thermo–hydro–mechanical behavior of the rock mass surrounding the cavern [7].

As an attempt to simplify this Computational Fluid Dynamics (CFD) problem, scientists tend to neglect the velocity field and the spatial variations of temperature and pressure over the cavern volume. This approach leads to a uniform cavern state where the thermodynamic variables (pressure and temperature) are functions of time only [8–14]. This simplification reduces tremendously the numerical weight of the problem and allows to better concentrate on other phenomena that take place in the well and the rock domain around the cavern. *He et al,* [10] provided a design approach to estimate the energy storage capacity of a fixed–volume cavern. Since they intended to concentrate on cavern operation schemes in isochoric uncompensated or isobaric compensated modes, as well as heat transfer conditions including isothermal, convective heat transfer, or adiabatic wall conditions, they developed a uniform thermodynamic model. In a similar framework, *Raju and Khaitan* [14] needed to validate their uniform thermodynamic model by properly calculating the heat transfer coefficient between the gas and the surrounding rock domain. For this purpose, they took the Huntorf plant as a case study and validated their simulations based on the plant's operating schemes. *Guo et al,* [9] tried to study the effect of the reservoir boundary permeability, specific heat, and thermal conductivity on the efficiency of compressed air storage systems. Therefore, they used a uniform thermodynamic model where they investigated pressure and temperature distributions due to different injection air temperature operations. There have been a few other papers where authors tried to account for the spatial variations in the cavern volume, however performed simulations were short (few hours) and other simplifications were implemented like the Boussinesq approximation [15–17]. *Barajas and Civan* [15] were concerned by studying the interactions of storage gas with the surface facilities through well and leaking into the rock formation. They developed a comprehensive CFD model and fully coupled it with the heat transfer approaches to calculate the temperature, pressure, and velocity fields in the underground caverns. However, simulations were short (24 hours), and pressure and temperature variations over the cavern volume did not exceed 1 MPa and 5 °C respectively.

The slow/seasonal cycling of underground caverns stems from the population's seasonal need of energy, where gas is stored in summer and extracted in winter. However, the increase of human energy demands, as well the environmental concerns associated, necessitate the use of viable and clean energy. Hydrogen storage in salt caverns represents a future fuel source. Nevertheless, the use of hydrogen as fuel requires fast utilization of the storage systems to respond to the daily demands of fuel required by the population [18]. Therefore, and due to the considerable simplifications usually adopted in the uniform thermodynamics modeling, a question always arises about the validity of such simplifications, especially during fast cycling of caverns when spatial variations of temperature and pressure are significant. The miscalculation of these variations leads to a miscalculation of the gas density field in the cavern, and consequently, for a given cavity volume, a misestimation of the stored gas mass.

To address this concern, we made use of an in–house simplifying code (DEMETHER [19]) and a CFD COMSOL license. The goal was to compare the simplified simulation results of DEMETHER, to the complex simulation results of COMSOL, where all complexities of the problem were considered, i.e. full mesh refinement, velocity field, convective heat transfer, and the turbulent flow modeling. The simulation results were correlated for both slow (seasonal) and fast (daily) cycling where one expects better match with regard to the slow cycling and more deviation in the case of fast treatment. In both simulations the cavern was assumed full of gas with no brine or insoluble material, and only thermal conduction with the surrounding rock domain was considered.

The paper proceeds as follows: the complete physical model for cavern thermodynamics was first presented along with the rock mass energy equation; the simplified uniform thermodynamic state technique was then discussed under the framework of the DEMETHER in–house code. The complete physical model with its complexities of meshing and turbulent flow was validated based on experimental results Appendix B. Once validations were verified, simulations on the cavern scale were run using the simplified and the complete approaches and simulation results were correlated for fast and slow cycling. The paper ends with a discussion section on the validity of this simplified approach. For a typical spherical cavern of volume 300,000 m^3 created at 910 m depth, severe cycling schemes that led to a mass change in the range of [-69% to -29%] of the initial mass, demonstrated almost similar results for slow/seasonal cycling between simplified and complete simulations. However, a difference margin of 7% was observed in the compared results during fast/daily treatment.

2. General thermodynamics of caverns

We will start by assuming an underground cavern filled with a mono–component single–phase fluid (Fig. 1). The fluid thermodynamic state can be defined either by (ν, T) or (p, T), with $\nu = 1/\rho$ (m^3/kg) and p (Pa) being the specific volume and pressure respectively, and T (K) is the temperature.

The underground storage system can be divided into three domains: 1) the well which extends from the ground surface to the cavern; 2) the cavern itself; and 3) the rock mass that surrounds the cavern and the well.

2.1. Complete solution of cavern thermodynamics

Injecting or withdrawing gas to/from caverns applies changes to the gas mass density ρ (kg/m^3), velocity $\boldsymbol{v}$, and temperature T. The developments of these three fields are calculated using the general balance laws:

$$\begin{array}{lrcl} \text{mass balance:} & \dot{\rho} + \rho\,\nabla.\boldsymbol{v} & = & 0; \\ \text{momentum balance:} & \rho\,\dot{\boldsymbol{v}} - \nabla.\underline{\underline{\boldsymbol{\sigma}}} & = & \rho\,\mathbf{g}; \\ \text{energy balance:} & \rho\,\dot{u} + \nabla\,.\,\boldsymbol{\psi} & = & \underline{\underline{\boldsymbol{\sigma}}} : \underline{\underline{\boldsymbol{\nabla}}}\boldsymbol{v}, \end{array} \tag{1}$$

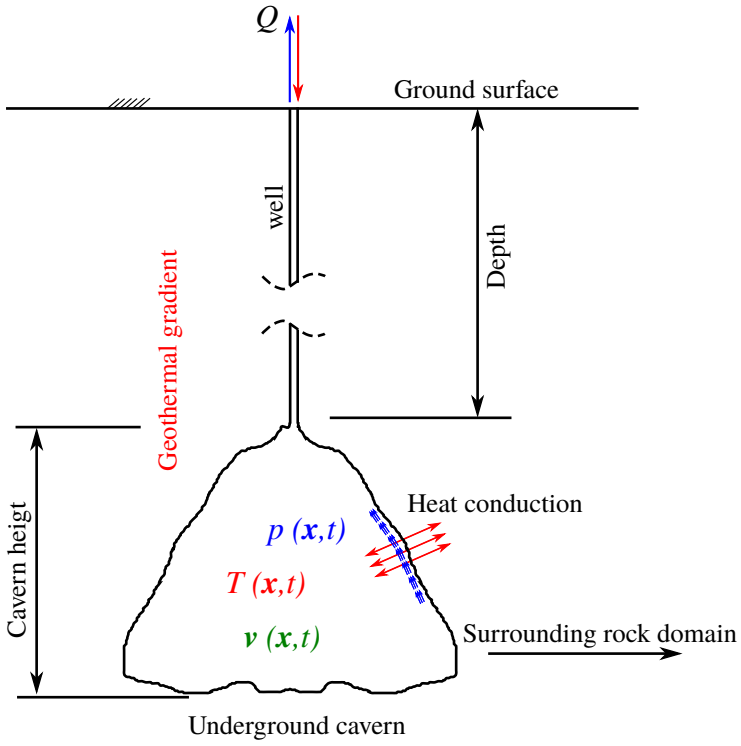

Figure 1: Schematic diagram of a typical underground cavern, $\boldsymbol{x}$ is the position vector at time t.

where $\underline{\underline{\boldsymbol{\sigma}}}$ is the fluid stress tensor (Pa), $\boldsymbol{g}$ the gravitational acceleration vector (m/s^2), u the specific internal energy (J/kg), and $\boldsymbol{\psi}$ the fluid heat flux (W/m^2). For any function $\varphi = \{\rho, \boldsymbol{v}, u\}$, the material derivative is expressed as $\dot{\varphi} = \partial_t \varphi + \boldsymbol{v}.\boldsymbol{\nabla}\varphi$.

Stocke's law is used to calculate the stress tensor in a moving fluid undergoing external effects,

$$\underline{\underline{\boldsymbol{\sigma}}} = 2\mu \underline{\underline{\boldsymbol{D}}}^d - p\underline{\underline{\boldsymbol{\delta}}}, \tag{2}$$

where μ is the fluid dynamic viscosity (Pa s), and $\underline{\underline{\boldsymbol{D}}}^d$ is the deviatoric part of the rate of strain tensor $\underline{\underline{\boldsymbol{D}}} = 0.5 \times \left(\underline{\underline{\boldsymbol{\nabla}}}\boldsymbol{v} + \underline{\underline{\boldsymbol{\nabla}}}\boldsymbol{v}^{\mathrm{T}}\right)$ (1/s). Fourier's law is used to describe the relation between heat flux $\boldsymbol{\psi}$ and the temperature gradient $\boldsymbol{\nabla}T$ (K/m) through the fluid effective thermal conductivity Λ (W/m/K),

$$\boldsymbol{\psi} = -\Lambda\, \boldsymbol{\nabla}T. \tag{3}$$

The fluid state equation can be completely described using two state functions; the mass density $\rho(p, T)$, and the heat capacity $C_p(T)$ (J/kg/K) at a given pressure [19]. The thermodynamic variables are related to each other through the formula $p = \rho\, T\, Z$, with Z being the gas compressibility factor. Common examples are when fluid density is assumed constant in case of incompressible fluids, and when $Z = R/M_w$ in case of ideal gases, with M_w being the gas molecular weight (kg/mol) and R (J/mol/K) the universal gas constant. In case of high pressure and low temperature, the assumption of ideal gas is weak and a real gas behavior needs to be considered.

As we will be conducting relatively short simulations (2 months maximum), we will neglect any mechanical behavior of the rock mass around the cavern [20], and we will consider only the thermal interaction between rock and fluid. For a time–dependent problem, the temperature field in the surrounding rock mass verifies the following form of the heat equation,

$$\partial_t T_s = \kappa_s \, \nabla.(\boldsymbol{\nabla} T_s), \tag{4}$$

with T_s and κ_s (m^2/s) being the rock temperature and thermal diffusivity respectively.

Heat convection regimes of a gas injected in or withdrawn from underground caverns can be either natural or forced. Natural convection corresponds to configurations where the gas flow is driven by buoyancy forces. Rayleigh number Ra is generally used to characterize the regime of natural heat convection. It is expressed as the ratio of buoyancy and viscosity forces multiplied by the ratio of momentum and thermal diffusivities [21],

$$\mathrm{Ra} = \frac{\text{Buoyancy forces}}{\text{Viscosity forces}} \times \frac{\text{Momentum diffusivity}}{\text{Thermal diffusivity}} = \frac{\rho^2 \, \mathrm{g} \, \alpha \, \Delta T \, L^3}{\mu^2} \times \frac{\mu \, C_p}{\Lambda} = \frac{\rho^2 \, \mathrm{g} \, \alpha \, C_p}{\mu \, \Lambda} \, \Delta T \, L^3, \tag{5}$$

where $\alpha = -\nu \, \partial_T \rho|_p$ is the isobaric volumetric thermal expansion coefficient (1/K), L is the cavity length over which flow takes place, g is the gravitational acceleration, and ΔT is a temperature difference usually set by the solids surrounding the fluid. When the Rayleigh number is small (typically $\mathrm{Ra} < 10^3$), convection is negligible and most of heat transfer occurs by conduction in the fluid. Besides, a turbulent model is necessary to fully describe the gas flow when Buoyancy forces are considerably high, i.e. $\mathrm{Ra} > 10^8$ [22].

The forced convection regime is observed when the flow is driven by external phenomena that dominate buoyancy effects. In this case the flow regime can be characterized using the Reynolds number as an indicator [23, 24],

$$\mathrm{Re} = \frac{\text{Inertial forces}}{\text{Viscous forces}} = \frac{\rho \, ||\boldsymbol{v}|| \, L}{\mu}, \tag{6}$$

with $||\boldsymbol{v}||$ being the magnitude of the fluid velocity. At low Reynolds numbers ($\mathrm{Re} < 2300$), viscous forces dominate and laminar flow is observed. At high Reynolds numbers ($4000 < \mathrm{Re} < 2300$), the damping in the system is very low, giving small disturbances. If the Reynolds number is high enough ($\mathrm{Re} > 4000$), the flow field eventually ends up in a turbulent regime. Most of the underground cavern operations exhibit high Reynolds $\mathrm{Re} \sim 10^6$ and Rayleigh $\mathrm{Ra} \sim 10^{15}$ numbers [25], which necessitates the integration of a fluid flow turbulent model to solve for velocity disturbances. Direct numerical simulations of turbulent flows using Navier–Stoke's equation are prohibitively expensive in terms of space and time discretization. This makes the use of eddy–viscosity models based on the Reynolds Averaged Navier–Stokes (RANS) equation quite common and acceptable in the CFD codes [26, 27]. In this work we will use the popular eddy–viscosity k-ϵ model [27–30] to account for flow turbulences, see Appendix A for details.

One last concern we may experience in the CFD simulations, is the forced heat convection term in the gas energy equation ($\boldsymbol{v}.\boldsymbol{\nabla}T$). This term can produce numerical instabilities that require special treatment. A thumb rule to quantify these produced numerical noises is the use of the Péclet number Pe,

$$\mathrm{Pe} = \frac{||\boldsymbol{v}||\, h_e}{2\,\kappa_f}, \tag{7}$$

where h_e is the averaged element size (m) and $\kappa_f = \Lambda/\rho\, C_p$ is the fluid thermal diffusivity (m^2/s). For a uniform mesh with first–order shape functions, it has been mathematically proven that numerical instabilities occur when $\mathrm{Pe} > 1$. The necessary consistent stabilization methods, i.e. Streamline and Crosswind Diffusion [31], will be applied when necessary to overcome numerical noise. During underground cavern simulations, natural heat convection is seen during the standstill/pause periods, however, forced convection is expected during injection and withdrawal cycling.

The evolution of the thermodynamic state of gas stored in underground caverns can be solved for by applying the finite element method on the system of Eqs 1 along with the proper initial and boundary conditions. However the following factors need to be considered:

1. the spatial discretization should be precise and fine enough to describe properly the distribution of the velocity field;
2. adequate mesh refinement must be adopted at the solid–fluid interface to account for the convective heat transfer;
3. a turbulent flow model is needed which adds another two variables, namely k and ϵ, to the list of unknowns.

This complete physical model with all related complexities of mesh refinement, spatial variations, convective heat transfer, and turbulent flow is validated in Appendix B.

2.2. Simplified solution of cavern thermodynamics

Underground caverns have large geometries and they are utilized over long periods of time. This renders the complete CFD simulations of gas cycling over their lifetime a tremendous if not a prohibitive task. Since in most cases, underground storage necessitates seasonal/slow cycling, scientists assume that cavern spatial variations of pressure and temperature to be negligible in the main part of the cavern volume [8–14]. Henceforth, they apply the concept of a heat transfer coefficient (λ_c) to account for solid–fluid heat exchange over the cavern surface,

$$\lambda_c = \frac{\text{Normal thermal conduction on the solid wall}}{\text{Temperature difference between solid and fluid}} = \frac{\boldsymbol{\psi}_s\,.\,\boldsymbol{n}_s}{T_s - T}, \quad (\mathrm{W/m^2/K}) \tag{8}$$

with $\boldsymbol{n}_s$ being the cavity inward normal vector and T the fluid temperature passing by the wall. Estimation of this coefficient is tedious, however, once *in situ* data is available, it can be precisely predicted [14].

In this paper, and as a simplistic approach that serves the comparison between the simplified and the complete solutions, a solid–fluid temperature continuity over the cavern surface was assumed. However, the well heat transfer coefficient (λ_w) was calculated using empirical laws.

As an example to this simplified uniform thermodynamic state approach, we are presenting our DEMETHER in–house FEM code. Based on the assumptions adopted by *Rouabhi et al,* [19] for pipe flow (constant cross section), the well velocity and thermodynamic variables are functions of time t and the curvilinear abscissa x along the well axis, i.e. $v(x,t)$, $T(x,t)$, and $p(x,t)$. For this case, the system of Eqs 1 becomes:

$$\begin{aligned} \rho\dot{\nu} - v' &= 0; \\ \rho\,\dot{v} + p' &= \rho\,\mathbf{g}\,.\,\boldsymbol{t} + (L_\zeta/\mathcal{A})\,\zeta_w; \\ \rho(\dot{u} + p\,\dot{\nu}) &= (L_w/\mathcal{A})\,\psi_w - v\,(L_\zeta/\mathcal{A})\,\zeta_w, \end{aligned} \tag{9}$$

where the prime denotes the variable derivative along the well axis, $\mathcal{A}$ is the flow cross sectional area (m^2), $\boldsymbol{t}$ is the vector tangent to the pipe wall, L_ζ is the well circumference available for fluid flow (m), and L_w is the well circumference available for heat transfer (m). These two circumferences are equal in the case of simple pipe flow. ψ_w is the heat exchange across the pipe wall, and ζ_w is the friction stress. The quantities ψ_w and ζ_w are usually given by empirical laws [32–34]. The stress ζ_w is generally expressed as $\zeta_w = -C_f \rho v|v|/2$. The term ψ_w implies the heat flux across the pipe wall, it can be expressed using the Newton's law as $\psi_w = \lambda_w(T_s - T)$. In the DEMETHER code, the following relations were adopted to calculate the empirical coefficients,

$$\begin{aligned} C_f &= 2\Big((8/\mathrm{Re})^{12} + (\mathrm{A}+\mathrm{B})^{-3/2}\Big)^{1/12}, \quad \text{with,} \\ A &= \left(-2.457\,\ln\Big((7/\mathrm{Re})^{0.9} + 0.27(\varepsilon L_\zeta/D_H)\Big)\right), \quad \text{and,} \quad B = (37530/\mathrm{Re})^{16}, \\ \mathrm{Nu} &= 3.66 \quad \text{for} \quad \mathrm{Re} \le 2300, \quad \text{and,} \\ \mathrm{Nu} &= (C_f/2)(\mathrm{Re}-1000)\mathrm{Pr}/\Big(1 + 12.7\sqrt{C_f/2}(\mathrm{Pr}^{2/3}-1)\Big) \\ &\quad \text{for} \quad 2300 < \mathrm{Re} < 5\times 10^6, \quad \text{and,} \quad 0.5 < \mathrm{Pr} < 2000, \end{aligned} \tag{10}$$

where ε is the wall roughness, $D_H = 4\mathcal{A}/L_\zeta$ (m) is the hydraulic diameter, Nu is the Nusselt number, $\mathrm{Pr} = \mu C_p/\Lambda$ is the Prandtl number. The pipe Reynolds number takes the form $\mathrm{Re} = \rho\, v\, D_H/\mu$. The well heat transfer coefficient is expressed in terms of the Nusselt number as $\lambda_w = \Lambda\,\mathrm{Nu}/D_T$, with $D_T = 4\mathcal{A}/L_w$ being the thermal diameter (m).

The problem is fully coupled in the sense that if the well variables are known, they can be used to determine the unknown parts of the boundary conditions of the cavern and the formation. Using these boundary conditions, the problem in the latest domains can be solved for leading to new data that can be put for a next time step solution. With regard to the cavern itself, assuming a uniform thermodynamic

state simplifies the system of Eqs 1 into:

$$\begin{aligned} \dot{M}/M &= -\alpha\,\dot{T} + \beta\,\dot{p}; \\ M\,C_p\,\dot{T} - V\,\alpha\,T\,\dot{p} &= Q_I(h_t^{\mathrm{w}} - h^{\mathrm{c}}) + \Psi_s, \end{aligned} \tag{11}$$

where M is the gas mass (kg), $\beta = \nu\,\partial_p\rho|_T$ is the isothermal compressibility factor (1/Pa), V is the cavity volume (m^3) (assumed constant), $h_t^{\mathrm{w}} = h^{\mathrm{w}} + \boldsymbol{v}\,.\,\boldsymbol{v}/2$ is the well dynamic/total enthalpy (J/kg), h^{c} is the cavern enthalpy (J/kg), Q_I is the inflow rate (kg/s), and $\Psi_s = \int_S \boldsymbol{\psi}_s\,.\,\boldsymbol{n}_s\,ds$ is the power exchanged between gas and the surrounding rock (W). With the assumption of solid–fluid temperature continuity over the cavern surface, this power exchange is calculated using the Fourier conduction equation in the rock formation side.

The assumption of a uniform thermodynamic state implies the neglection of spatial variations and velocity field in the system of Eqs 11. This leads to considerable simplifications to the mathematical problem. Considering that the time derivatives do not account for convective terms any more, and that the main variables are only functions of time, the system of Eqs 11 represents a system of ordinary differential equations of $p(t)$ and $T(t)$. The complexities left stem from the necessity to model a real gas behavior (when necessary and appropriate), and the discretization needed in the rock domain to solve for Eq. 4. However, since the cavern thermodynamic behavior is now assumed uniform in its domain (single point behavior), the surrounding rock mass is discretized into finite elements and heat conduction is assumed one–dimensional.

3. Simulations on the cavity scale

The boundary value problem represents a spherical cavity of volume $V = 300,000\ \mathrm{m}^3$ in a surrounding rock domain. The well extends from the surface at $z = 0$ m to the cavity at $z = z_w = -910$ m. The initial cavity volume averaged temperature and pressure are 40 °C and 22 MPa respectively (Fig. 2). Gas is injected at $T = 40$ °C following the program shown in Fig. 3. The gas used in the simulations is ideal hydrogen[1] and the cavern is assumed initially full with mass $M(0) = 4.52 \times 10^6$ kg.

Figure 3 shows the injection schemes that will be considered in our simulations in terms of relative mass change $\tilde{M} = (M/M(0) - 1) \times 100\%$. The first scheme represents fast/daily cycling where our cavern is utilized extensively, and one cycle (4.5 days) leads to a relative mass change in the range [-69% to -29%]. Second scheme represents slow/seasonal cycling utilization where the cavern experiences the same relative mass change, yet over a period of 58.5 days. There are periods of standstill/rest/pause after injection and withdrawal that are marked by constant relative mass change over time. Simulations are run for 60 days to allow for the investigation of thermal exchange between gas in the cavern and the surrounding rock

[1] The assumption of ideal gas simplifies calculations considerably.

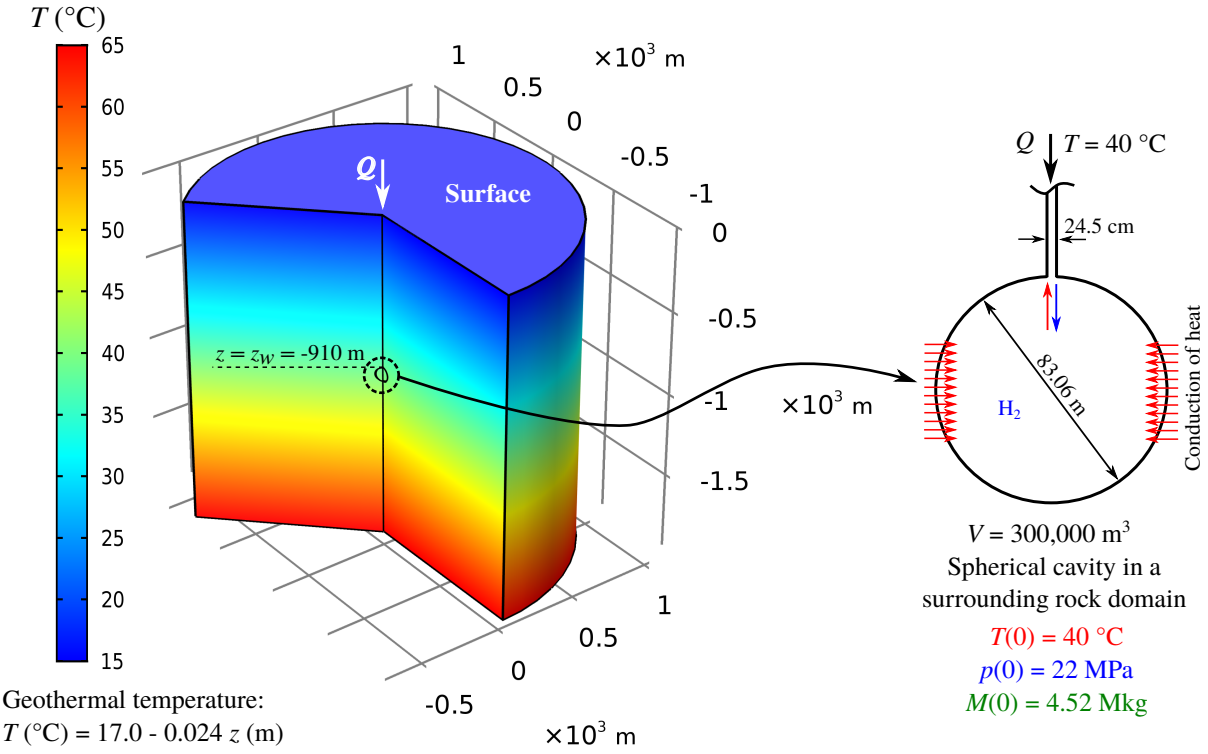

Figure 2: Schematic diagram of the boundary value problem: it represents a spherical cavern created at depth 910 m in a surrounding rock domain. The geothermal gradient gives a cavern volume averaged temperature of 40 °C. The cavern is assumed initially full of ideal hydrogen with mass $M(0) = 4.52 \times 10^6$ kg at $p(0) = 22$ MPa.

mass. Points p_1 of withdrawal at $(t = 6.332, \tilde{M} = -57.6)$, p_2 of injection at $(t = 25.87, \tilde{M} = -51.73)$, and p_3 of pause at $(t = 35.66, \tilde{M} = -29.03)$ are displayed on the figure where velocity and temperature profiles are to be analyzed in the coming arguments.

The gas cycling in the spherical cavern shown in Fig. 2 is to be simulated using DEMETHER and COMSOL, then results of these softwares will be correlated for fast and slow cycling. As such simulations can be performed using other softwares, and for the purpose of generalizing the objective of this work, we shall be referring to DEMETHER as the simplified approach and to COMSOL as the complete approach. For the complete simulations, the boundary conditions are set as shown in Fig. 2. The rock formation far–field temperature boundary conditions were assumed to be of the Dirichlet type, i.e. $T = T_\infty(z)$, with $T_\infty(z)$ being the initial geothermal temperature. In case of the simplified simulations, $T_\infty(z)$ is replaced by its average over the cavern surface. Gas is injected at $T = 40$ °C following the two schemes of Fig. 3. As for the initial conditions, in the complete simulations, the well and cavern are assumed in equilibrium with the surrounding rock $T(\boldsymbol{x}, 0) = T_\infty(z)$. However, in the case of simplified simulations, the cavern temperature is set to $T(0) = 40$ °C. Yet, the same temperature gradient (Fig. 2) is applied over the well length.

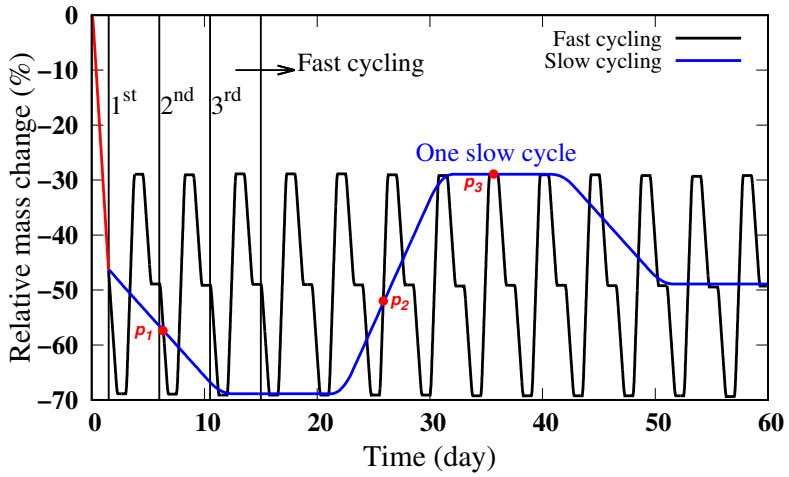

Figure 3: Two cycling schemes to run our cavern: fast/daily cycling that leads to a relative mass change of [-69% to -29%] in 4.5 days; and slow/seasonal cycling where cavern experiences the same mass changes yet over a period of 58.5 days. Points p_1 of withdrawal, p_2 of injection, and p_3 of pause, are displayed on the figure to investigate velocity and temperature profiles in the coming discussions.

Figure 4 shows the 2–D axysemtrical discretization of our boundary value problem for the complete simulations. The mesh consists of 445304 elements of which 24607 quadrilateral boundary elements to account for solid–fluid heat transfer and turbulent flow. Aside from the boundary layer quadrilateral elements, we made sure that the well be discretized into at least another 5 triangular elements to solve for possible radial variations of its thermodynamic quantities. At this level of discretization, solution was not mesh dependent, and the values of wall function δ_w^+ were in accordance with recommendations for good accuracy [27, 36]. For the comparison purpose, a similar one–dimensional discretization with 5000 elements was used in the simplified simulations for the rock domain, and the well was discretized into 1000 elements over its length. Rock thermal diffusivity was set equal to $\kappa_s = 0.29 \times 10^{-5}$ m^2/s. Ideal hydrogen was assigned the following thermodynamic properties: $\Lambda = 0.195$ W/m/K; $C_p = 10225$ J/kg/K; and $\mu = 8.75 \times 10^{-6}$ Pa s.

Figure 5 shows the development of the complete simulations volume averaged and the simplified approach temperature and pressure histories in the cavern during the slow and fast cycling schemes. Since pressure histories are mainly affected by mass changes, simplified and complete pressure histories are too much comparable (Figs 5(a, c)). However, and with regard to temperature histories, temperature histories show very slight differences in the case of slow cycling (Fig. 5(b)), yet differences are noticeable in the case of fast cycling and they increase with time to stabilize eventually (Fig. 5(a)).

To further comment on the efficiency of the simplified approach, the temperature and the vertical gas velocity profiles along the treatment well were compared. A pipe model for the well simulations in the simplified approach was used, and the solid–fluid interaction was accounted for using empirical laws. In

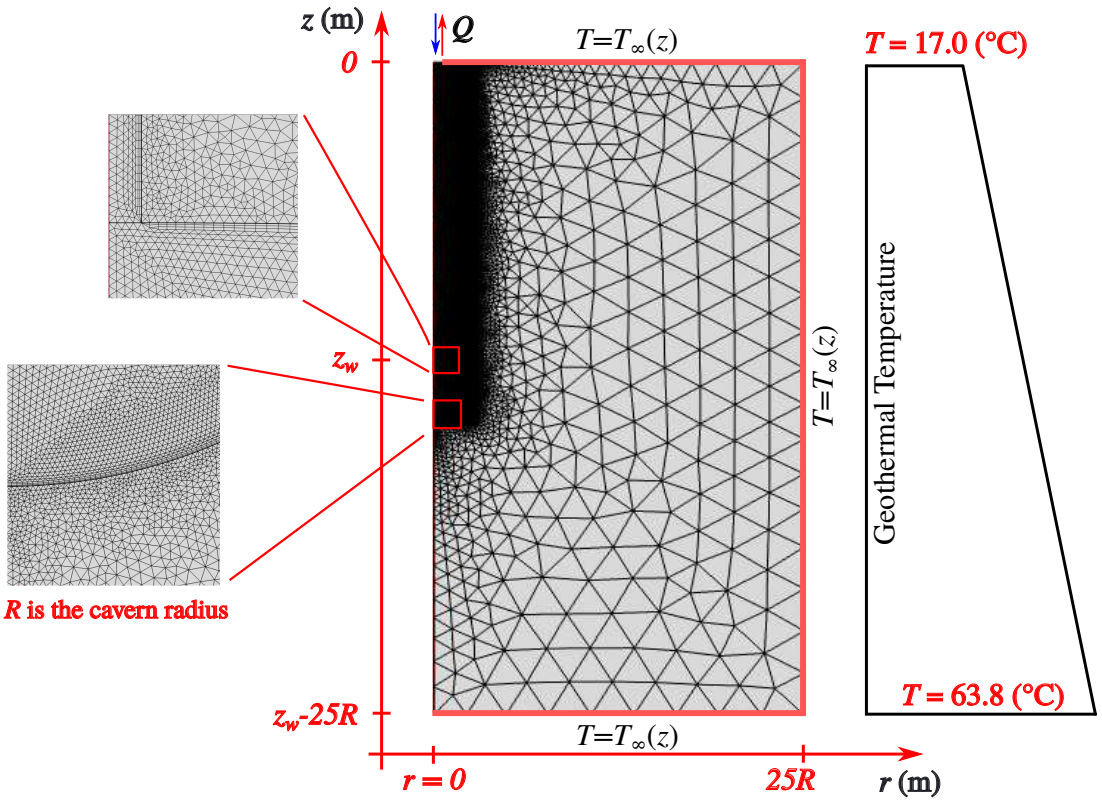

Figure 4: 2–D axysemtrical discretization of the boundary value problem of Fig. 2 for complete simulations. A surrounding rock volume of $25R$ is chosen around the cavity and well to avoid the effect of far–field boundaries. Mesh is considerably refined on the solid–gas boundary with quadrilateral boundary elements based on the recommendations of the k-ϵ turbulent flow. Mesh is also heavily refined for a certain volume in the rock domain around the cavity and well to better account for the large changes happening close to them in the time frame of our simulations (60 days). Mesh contains 445304 elements of which 24607 quadrilateral boundary elements.

the case of the complete simulations, only extensive and appropriate mesh refinement was implemented all through the model to calculate the velocity field and the convective heat transfer.

Figures 6(a, b, c) show the well temperature and velocity profiles in the complete (dashed–dotted lines) and the simplified (solid lines) approaches during slow cycling at points p_1 (withdrawal), p_2 (injection), and p_3 (standstill) of Fig. 3 respectively, and Figs 6(d, e, f) show the same profiles yet during fast cycling. It is clear that these profiles are quite comparable in the case of slow cycling, where velocity profiles are almost vertical, meanwhile temperature profiles show a curving behavior depending on the state of treatment (withdrawal or injection). In the case of pause/standstill, velocity is equal to zero, and temperature profiles show linear variations and tend to resemble the natural geothermal temperature profile. In the case of fast cycling (Figs 6(d, e, f)), and even–though velocity profiles are to some point comparable, temperature profiles are considerably different and they do not show the curving variations anymore due to the fast treatment. In the case of the complete approach, well profiles were calculated

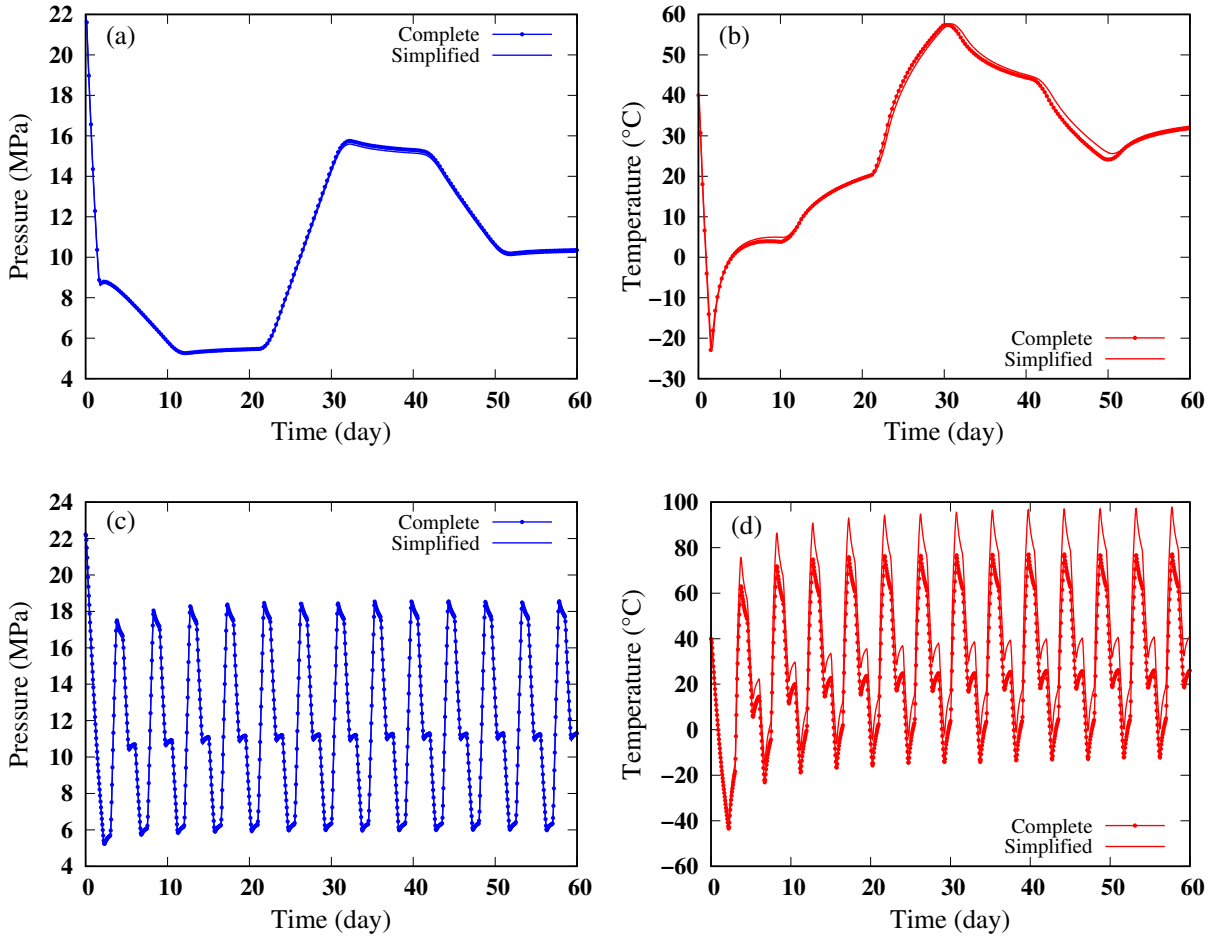

Figure 5: Development of cavity pressure and temperature: comparison between slow/seasonal (a, b) and fast/daily (c, d) cycling of the simplified and the complete approaches.

along its central line, however in the simplified simulations, there were no radial variations due to the application of 1–D pipe model.

As the complete simulations for fast and slow cycling are already performed, it is of interest to compare the velocity, the temperature, and the pressure heterogeneities in the cavern volume during these treatments. Figure 7 shows the contours of gas velocity magnitude at points p_1, p_2, and p_3 for the same value range of [0 to 0.2] m/s. One can see that, regardless of the treatment stage, gas velocity is significant by the cavern wall. However, in case of injection, velocity becomes also large near the injection well and it goes all through the cavern volume for fast cycling, yet considerable values never hit the cavern bottom for the case of slow cycling. It is also evident that a larger cavern volume is affected by the gas velocity heterogeneities throughout the fast cycling scheme.

The heterogeneities in the velocity field are expected to create corresponding heterogeneities in the

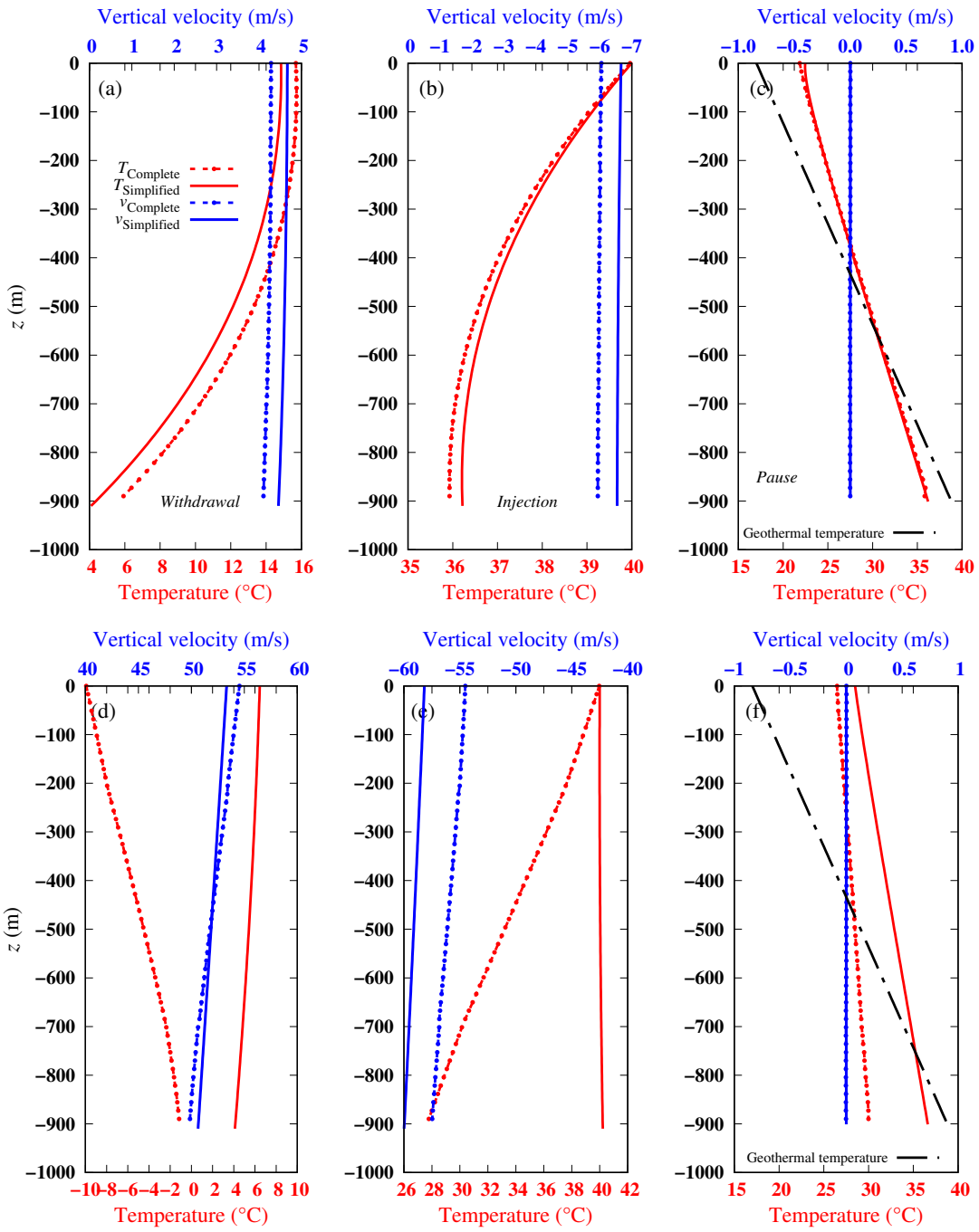

Figure 6: Development of well temperature and gas velocity profiles during slow cycling (figures a, b, and c), and during fast cycling (figures c, d, and e), at points p_1 of withdrawal, p_2 of injection, and p_3 of pause respectively (Fig. 3). The figure compares the simulation results of the complete and the simplified approaches.

temperature field (Fig. 8).

Such temperature heterogeneities are radial and vertical following gas flow patterns. Nevertheless, this

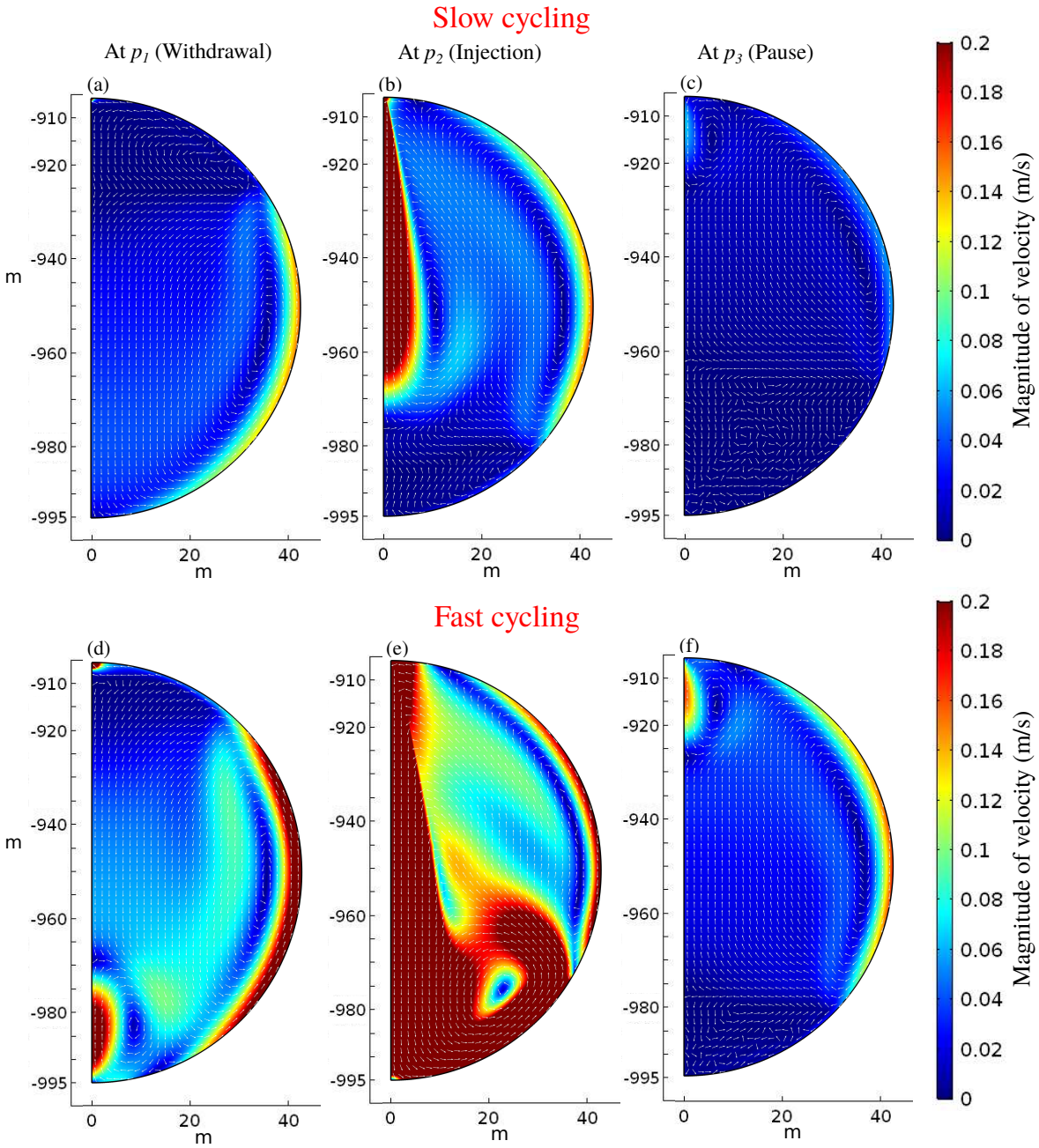

Figure 7: Contours of the magnitude of gas velocity vector $||\boldsymbol{v}||$ (m/s). The figure compares the results of slow and fast cycling at points p_1, p_2, and p_3 for the same value range of [0 to 0.2] m/s. White arrows show the gas flow patterns.

is not the case in the pressure contours where variations are almost vertical and are typically attributed to the gas weight (Fig. 9).

As to quantify the spatial variations of velocity, temperature, and pressure over the time course of simulations, the radial and vertical components of these fields were averaged over the cavern volume (Fig.

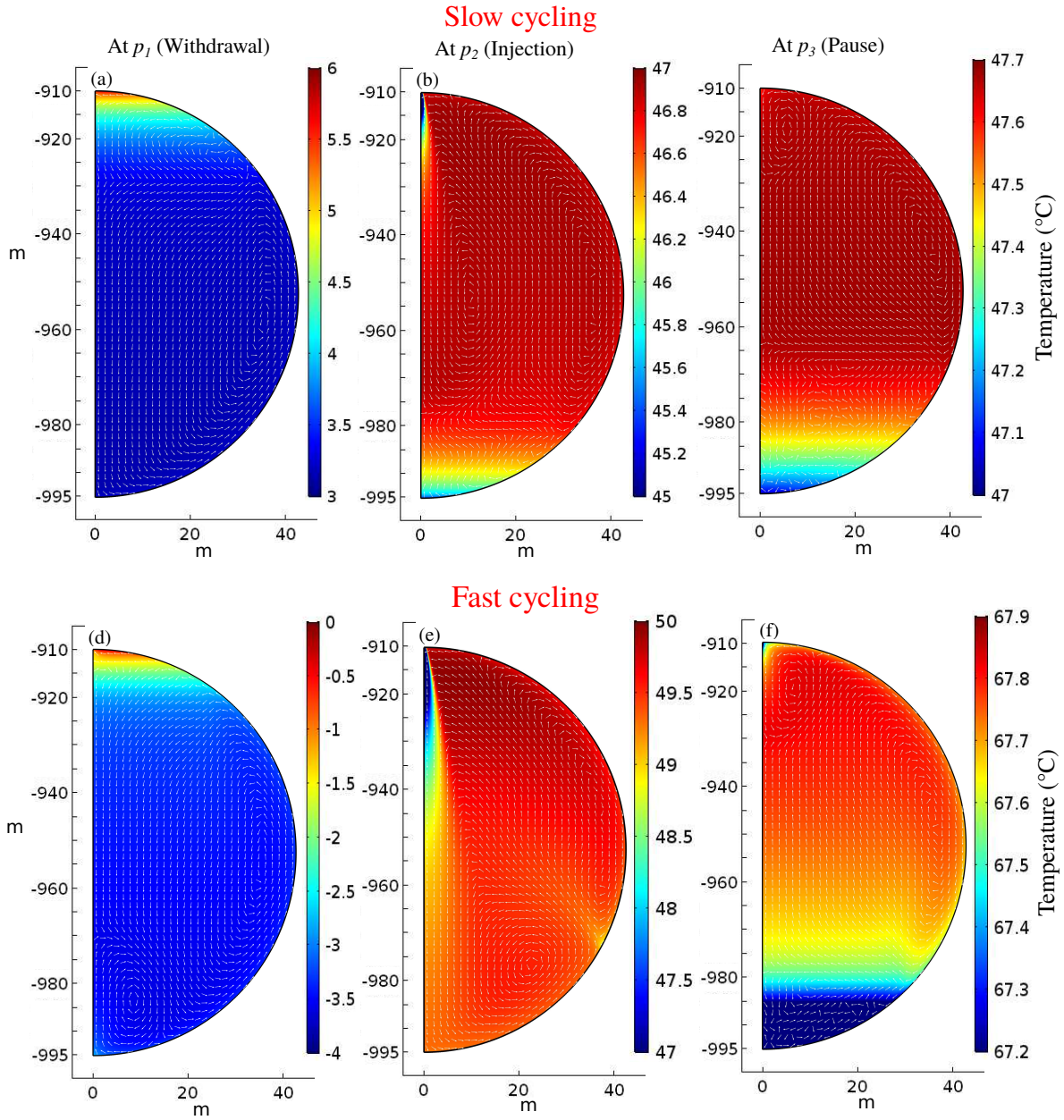

Figure 8: Contours of temperature T (°C). The figure compares the results of slow and fast cycling at points p_1, p_2, and p_3. White arrows show the gas flow patterns.

10) for fast and slow cycling.

The spatial variations of the velocity field create spatial variations in the other thermodynamic variables fields. In the case of vertical components, velocity variations are three–fold larger in case of fast cycling, and for radial components, the fast cycling variations are one order of magnitude higher (Figs 10(a, b)). This affects significantly the radial and vertical variations of the temperature field. Such variations are observed to be at least three-fold higher for fast cycling treatment (Figs 10(c, d)). Nonetheless,

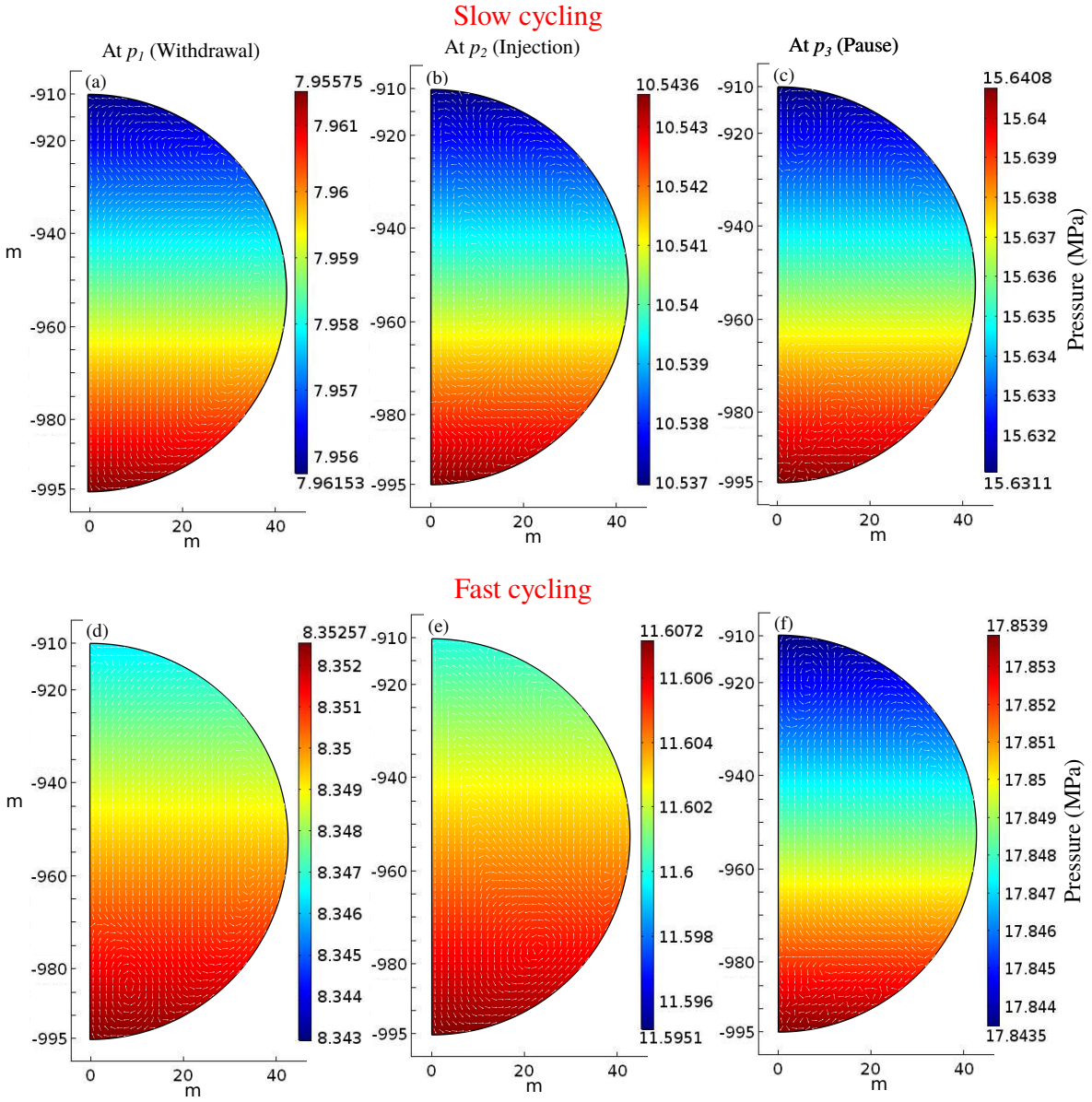

Figure 9: Contours of pressure p (MPa). The figure compares the results of slow and fast cycling at points p_1, p_2, and p_3. White arrows show the gas flow patterns.

radial variations of the pressure field are negligible, and vertical variations are almost comparable between fast and slow cycling (Figs 10(e, f)). Vertical pressure variations are mainly related to the gas weight and they are still negligible when compared to the volume averaged values in the range of [5 to 18] MPa. These spatial variations in the three fields create the solution differences between the simplified and the complete approaches (Fig. 5).

As to investigate the validity of implementing a turbulent flow model even at the level of slow cycling, Fig. 11 shows the development of the volume averaged Reynold's and Rayleigh numbers during the course

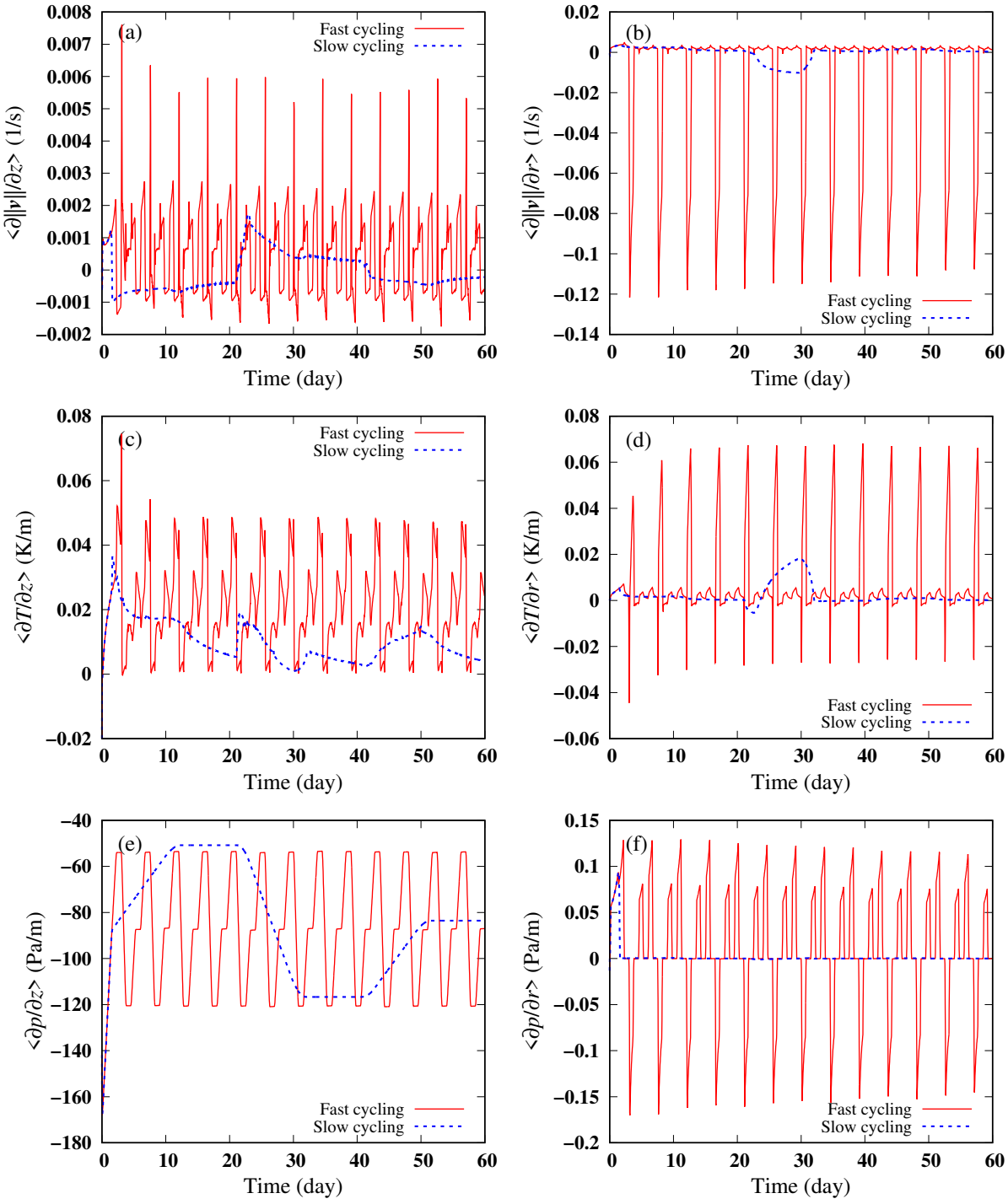

Figure 10: Volume averaged spatial variations of the velocity field magnitude (a, b) (1/s), of the gradient of temperature field (c, d) (K/m), and of the gradient of pressure field (e, f) (Pa/m).

of slow cycling. The figure also shows time–course of the maximum and minimum possible values within the cavern volume.

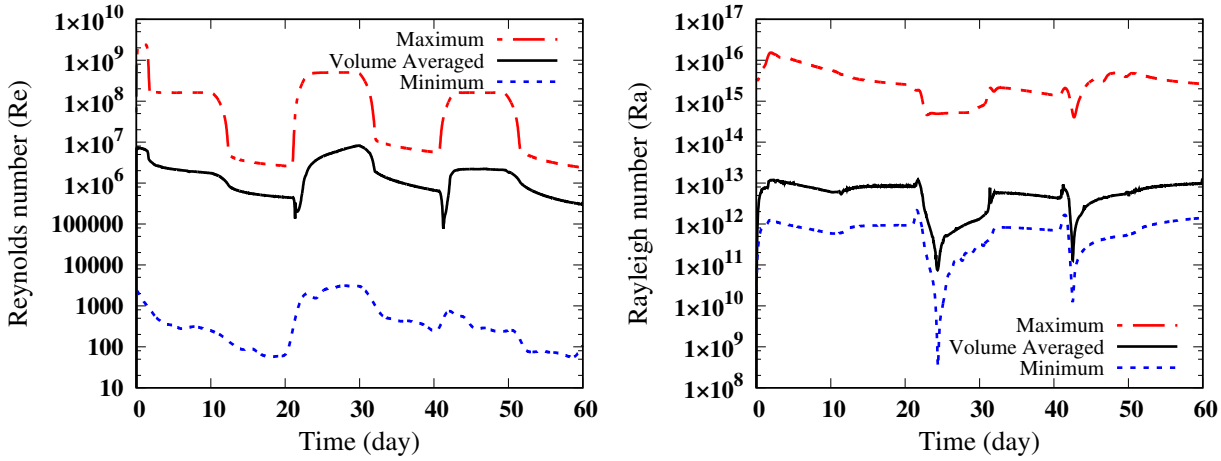

Figure 11: Development of the volume averaged Re and Ra numbers during the course of slow cycling. The figure also shows time–course of the maximum and minimum possible values within the cavern volume.

The cavern volume averaged values (Fig. 11) indicate that at most of the spatial positions, and for the majority of the simulation time, a turbulent flow model is required. The turbulent $k-\epsilon$ model used in this paper will still give appropriate results if flow turns out to be laminar at some locations. High values of these dimensionless numbers are related to the low dynamic viscosity of hydrogen.

The Biot number is another dimensionless number that we can use to quantify the heat transfer part of our problem [35]. This number relates the conductive resistance of the rock domain to the convective resistance of gas inside the cavern, i.e. $\mathrm{Bi}_c = (\ell/\Lambda_s)/(1/\lambda_c) = \lambda_c\,\ell/\Lambda_s$, with $\ell = \sqrt{\kappa_s\, t}$ being the thermal penetration depth into the rock domain. To calculate the Biot number over the cavern surface, Eq. 8 was used while setting the fluid temperature equal to the cavern center temperature, while heat flux and solid temperature were averaged over the cavern surface, i.e. $\lambda_c = \langle \boldsymbol{\psi_s} \,.\, \boldsymbol{n}_s \rangle_{\mathrm{Surface}} / (\langle T_s \rangle_{\mathrm{Surface}} - T_{\mathrm{Center}})$. Fig. 12(a) shows the development of λ_c during the treatment course, where unlike the case of slow cycling, it does not vary a lot during the fast cycling course.

Knowing the cavern heat transfer coefficients for fast and slow cyclings, a maximum value of $\mathrm{Bi}_c \approx 14.0$ is observed in the case of fast cycling and that of approximately 5.0 in the case of slow cycling (Fig. 12(b)). A lesser value of Biot number means a more convective resistance (smaller λ_c), which indicates a more uniform cavern temperature distribution that interprets a good correlation between the simplified and the complete simulations.

Figure 13 compares the radial temperature distribution in the rock domain for the simplified and the complete simulations and during fast and slow cycling at points p_1 (withdrawal), p_2 (injection), and p_3 (standstill) of Fig. 3 . In the complete simulations, profiles are tracked at the cavern wall at the cylindrical coordinates ($r = R,\ z = z_w - R$ m). The one–dimensional discretization in the simplified simulations was sufficient to reproduce identical thermal distribution to the complete simulations (Fig.

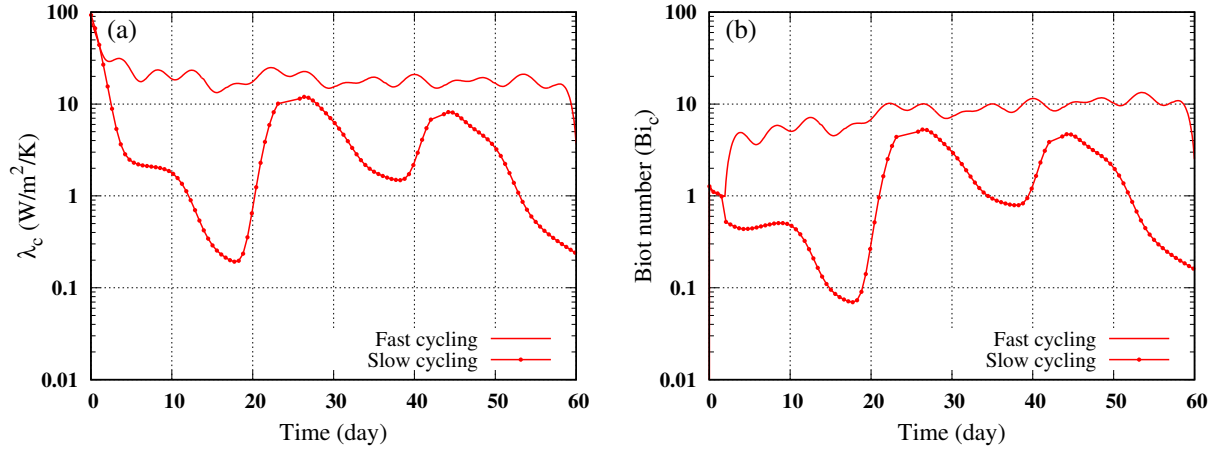

Figure 12: Development of the cavern heat transfer coefficient (a) and Biot number (b) during the course of fast and slow cyclings.

257 13(b)). However, considerable discrepancies are observed in the case of fast cycling (Fig. 13(a)).

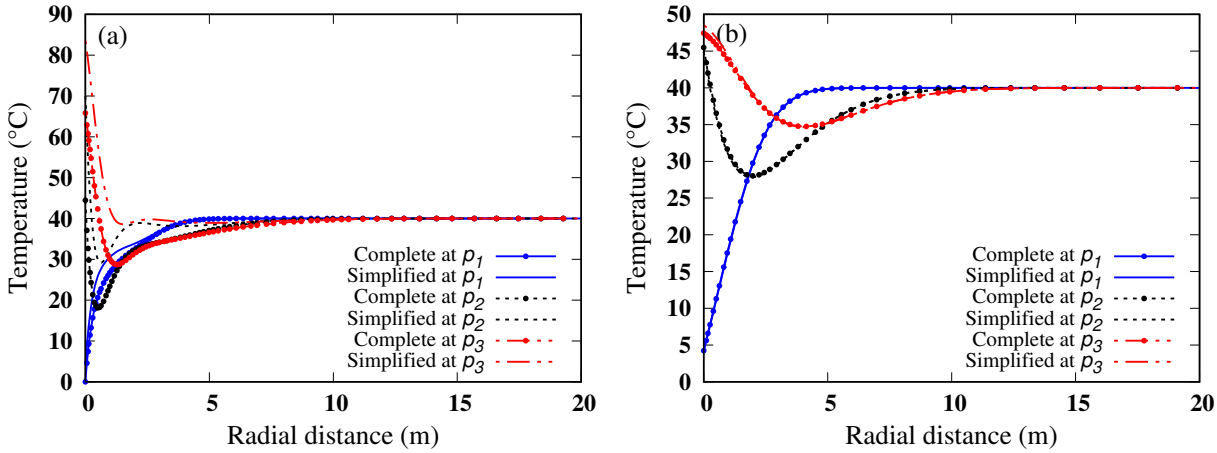

Figure 13: Radial temperature distribution in the rock domain: the figure compares between the simplified and the complete simulations for the cases of fast (a) and slow cycling (b) and at points p_1 (withdrawal), p_2 (injection), and p_3 (standstill) of Fig. 3.

258 Similarly, Fig. 14 shows the power exchanged between the gas in the cavern and the rock domain
259 during fast and slow cycling and for complete and simplified simulations. The figure demonstrates almost
260 an identical gain and loss of energy in the case of slow cycling for complete and simplified simulations
261 (Fig. 14(b)). However, noticeable discrepancies are clear in the case of fast cycling, where simplified
262 approaches tend to overestimate the energy loss to the rock domain during injection (Fig. 14(a)).

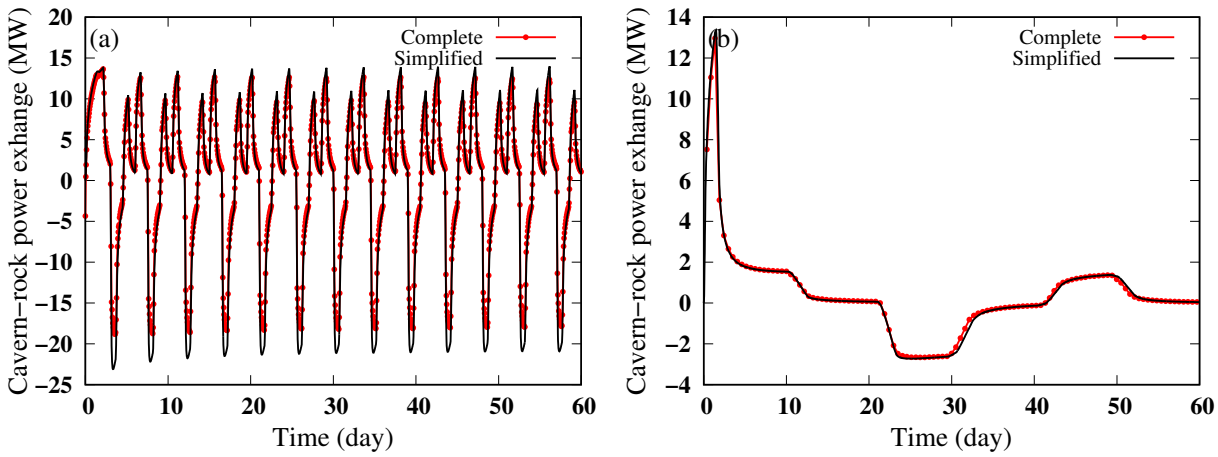

Figure 14: Development of the power exchanged between gas and the rock domain: the figure compares between the simplified and the complete simulations for the cases of fast (a) and slow cycling (b).

4. Discussion and conclusion

The objective of this research was to know to which level the simplified uniform thermodynamic state simulations of gas storage in underground caverns (used generally) could be valid, by comparing it to complete simulations that would address all the complexities of the problem, i.e. mesh refinement, gas velocity field, turbulent flow model, and convective heat transfer. As we had access to an in–house simplified code (DEMETHER) and CFD COMSOL license, two simulations of fast and slow cycling were launched. It was perceived initially that if spatial variations of the thermodynamic variables were small to a certain point, complex simulations could correlate to the simplified approach.

Figure 15 shows the absolute value of the relative Kelvin temperature difference ($|1-T_{\text{Complete}}/T_{\text{Simplified}}|\times 100\%$) between complete and simplified simulations of Figs 5(b, d).

In the case of slow cycling, relative differences are quite small and do not exceed 1%. However, these differences increase over time in the case of fast cycling, yet they tend to reach a maximum plateau of 7%. The increase over time is related to temperature exchange with the rock mass, where the gas velocity by the cavern wall drives the convective heat transfer.

Eventually, and despite considering all possible complexities of the problem, the simplified slow cycling simulations for both well profiles (Figs 6(a, b, c)) and cavern histories (Fig. 5), were quite close to the complete simulations with relative differences that did not exceed 1%. In terms of calculation times, simplified simulations (the DEMETHER code in this case) did not last longer than 2 hours, however, complete simulations (COMSOL) for fast cycling took approximately 60 days, and for slow cycling 45 days on parallel computation server of 16 cores. There are still more obvious differences between complete and simplified results in the case of fast cycling that reach relative differences of 7%. Though well velocity

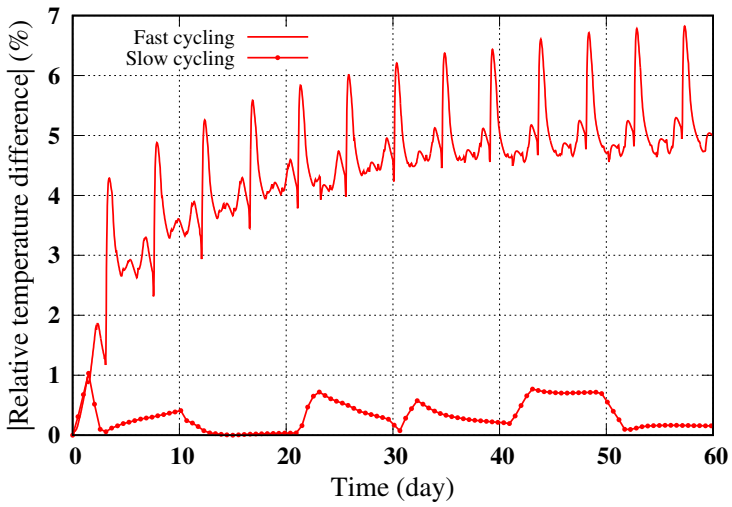

Figure 15: Relative Kelvin temperature difference $|1 - T_{\text{Complete}}/T_{\text{Simplified}}| \times 100\%$: comparison between complete and simplified simulations for fast and slow cycling of Figs 5(b, d).

profiles were comparable, temperature profiles were considerably different, which renders the use of such simplified approaches questionable in the case of fast cycling.

It is understood that a trade–off between accuracy and the calculation time is to be made. It is, until this time, still unfeasible to run complex complete simulations over the entire cavern lifetime, i.e. 30 years and maybe more. Yet, the simplified approaches can give out results in a few days. In the case of seasonal utilization of underground caverns, i.e. gas is stored in summer and withdrawn in winter, the simplified simulations are quite efficient in terms of results and the calculation cost. In addition to that, such simplified approaches allow researchers to concentrate on/address other problems that are of significant importance to the industry, of which we might cite the thermo–hydro–mechanical behavior of the rock mass during cycling, real gas behavior, interactions between the cavity species (gas, brine, and insoluble material), multi–phase simulations, and gas diffusion/loss into the rock mass. Still, while modern humanity demands on energy increase, the simplified approaches, to a certain level, will impose a definite level of inaccuracy that might be unacceptable. The miscalculation of the cavern thermodynamic variables development will lead to misestimation of the stored gas mass, as an example.

Acknowledgment

The authors would like to thank Prof. Michel Tijani, Dr. Joël Billiotte, and Dr. Faouzi Hadj–Hassen (MINESParisTech) for their valuable efforts in bringing out this work.

Appendix A.

The k-ϵ turbulent flow model

A turbulent model is necessary to fully describe gas flow in underground caverns especially when inertial forces are high, i.e. Ra $> 10^8$ and Re > 4000 [26]. One of the most popular and used eddy–viscosity models is the k-ϵ model [27–29]. It is a two–equation model which gives a general description of turbulence by means of two transport partial differential equations:

1. the first transported variable determines the energy in the turbulence and is called turbulent kinetic energy k ($\mathrm{m}^2/\mathrm{s}^2$);
2. the second transported variable is the turbulent dissipation ϵ ($\mathrm{m}^2/\mathrm{s}^2/\mathrm{s}$) which determines the rate of dissipation of the turbulent kinetic energy.

In our research this model is implemented by applying the following definitions into Eqs 2 and 3:

- μ and Λ are replaced by there effective values;

$$\begin{aligned} \mu_{\mathrm{eff}} &= \mu + \mu_t; \\ \Lambda_{\mathrm{eff}} &= \Lambda + \Lambda_t; \end{aligned} \tag{A.1}$$

  where μ_t and Λ_t are the turbulent/eddy parts of the dynamic viscosity and of the thermal conductivity, defined as,

$$\mu_t = \rho \, \frac{C_\mu \, k^2}{\epsilon}, \quad \Lambda_t = \frac{\mu_t \, C_p}{\sigma_T}, \tag{A.2}$$

  with C_μ and σ_T being empirical coefficients,

- stress tensor in Eq. 2 is replaced by a modified quantity;

$$\underline{\underline{\boldsymbol{\sigma}}}^{\mathrm{m}} = 2\mu_{\mathrm{eff}} \, \underline{\underline{\boldsymbol{D}}}^d - \left(p + \frac{2}{3} \rho \, k \right) \underline{\underline{\boldsymbol{\delta}}}, \tag{A.3}$$

- the instantaneous velocity field $\boldsymbol{v}$ is expressed as the sum of an average part $\bar{\boldsymbol{v}}$ and turbulent part $\boldsymbol{v}'$, i.e. $\boldsymbol{v} = \bar{\boldsymbol{v}} + \boldsymbol{v}'$. The kinetic energy of turbulence k ($\mathrm{m}^2/\mathrm{s}^2$) and its dissipation rate ϵ ($\mathrm{m}^2/\mathrm{s}^2/\mathrm{s}$) are defined by averaging the turbulent part of the velocity field;

$$k = \frac{1}{2} \, \overline{\boldsymbol{v}' \, . \, \boldsymbol{v}'}, \qquad \epsilon = \frac{\mu}{\rho} \, \overline{\underline{\underline{\boldsymbol{\nabla}}} \boldsymbol{v}' : \underline{\underline{\boldsymbol{\nabla}}} \boldsymbol{v}'^{\mathrm{T}}}, \tag{A.4}$$

  and are obtained by solving their respective transport equations,

$$\rho \, \partial_t k + \rho \, \boldsymbol{v} \, . \, \boldsymbol{\nabla} k = \nabla \, . \, \boldsymbol{\psi}_k + P - \rho \, \epsilon, \tag{A.5}$$

  and,

$$\rho \, \partial_t \epsilon + \rho \, \boldsymbol{v} \, . \, \boldsymbol{\nabla} \epsilon = \nabla \, . \, \boldsymbol{\psi}_\epsilon + C_1 \, \frac{\epsilon}{k} \, P - C_2 \, \rho \, \frac{\epsilon^2}{k}, \tag{A.6}$$

with $\boldsymbol{\psi}_k$ and $\boldsymbol{\psi}_\epsilon$ being the diffusion fluxes of k and ϵ and are defined as,

$$\boldsymbol{\psi}_k = \left(\mu + \frac{\mu_t}{\sigma_k}\right)\boldsymbol{\nabla} k, \qquad \boldsymbol{\psi}_\epsilon = \left(\mu + \frac{\mu_t}{\sigma_\epsilon}\right)\boldsymbol{\nabla}\epsilon. \tag{A.7}$$

The turbulent kinetic energy produced by shear P is modeled as,

$$P = \mu_t\Big[\underline{\underline{\boldsymbol{\nabla}}}\boldsymbol{v} : (\underline{\underline{\boldsymbol{\nabla}}}\boldsymbol{v} + \underline{\underline{\boldsymbol{\nabla}}}\boldsymbol{v}^{\mathrm{T}}) - \frac{2}{3}(\nabla\,.\,\boldsymbol{v})^2\Big] - \frac{2}{3}\,\rho\,k\,\nabla\,.\,\boldsymbol{v}. \tag{A.8}$$

The k-ϵ empirical quantities C_μ, C_1, C_2, σ_k, σ_ϵ, and σ_T, are assigned the following values respectively [27–29], 0.09, 1.44, 1.92, 1.0, 1.3, and 0.9.

Near the model walls, Reynold's number is rather small and viscous effects dominate which renders the k-ϵ equations invalid. Consequently, the problem cannot be described completely unless shear viscous stresses are defined on the wall as well as the necessary boundary conditions for the k-ϵ model. For this cause, *Kuzmin et al,* [27] and *Lacasse et al,* [36] provided analytical solutions of the boundary layer equations while assuming non–slip conditions. The non–slip condition makes the velocity vector tangent to the wall, i.e. $\boldsymbol{v}\,.\,\boldsymbol{n} = 0$. The balance equation of the tangential viscous forces exerted by the turbulent stress tensor is given by,

$$\left[2\mu_{\mathrm{eff}}\,\underline{\underline{\boldsymbol{D}}}^d - \frac{2}{3}\rho\,k\,\underline{\underline{\boldsymbol{\delta}}}\right]\boldsymbol{n} = -\rho\,\frac{u_\tau}{u^+}\,\boldsymbol{v}, \tag{A.9}$$

with,

$$\boldsymbol{\nabla} k\,.\,\boldsymbol{n} = 0, \quad \text{and,} \quad \epsilon = \rho\,\frac{C_\mu\,k^2}{\mu\,\chi_{\mathrm{v}}\,\delta_w^+}, \tag{A.10}$$

where $u_\tau = C_\mu^{1/4}\sqrt{k}$ is the wall friction speed (m/s), and $\chi_{\mathrm{v}} = 0.41$ is the von Kármán constant. u^+ and δ_w^+ are the model wall functions that take into account the discretization near the wall as well as the gap size between the wall and the turbulent flow domain. COMSOL adopts the same relations for these functions as can be found in literature [27, 36], and it gives δ_w^+ as a result and an analysis variable. It is required, for good accuracy, that this parameter be equal to 11.06 on most of the walls.

Once k and ϵ are known by solving their transport equations, the effective parameters of Eq. A.1 are calculated by substituting for their turbulent parts. Subsequently, the conservation equations of cavern thermodynamics are solved for using these effective parameters and the modified stress tensor. The use of the k-ϵ model requires specific considerations and it has its certain limitations:

1. simulations start by describing a laminar flow regime until time $t = t_L$ and the turbulent flow model is activated for $t > t_L$. The initial values of turbulent kinetic energy k_0 and its dissipation ϵ_0 are assigned depending on the laminar dynamic viscosity [27];

2. the k-ϵ model requires equilibrium in the boundary layers. Consequently, it does not respond correctly to flows with adverse pressure gradients. This is not common in the case of gas flow since pressure spatial variations are rather small and can generally be neglected when compared to the cavern volume values (Figs 10(e, f));
3. there are some numerical constraints with regard to the mesh refinement near walls. Relatively small elements need to be used in the boundary layers and numerical solutions are to be investigated so that accuracy can not be considerably compromised [36, 37].

Appendix B.

Validation on the laboratory scale

This appendix aims at validating the thermodynamic framework (Eqs 1) and particularly the k-ϵ model for turbulent flow (Appendix A) using laboratory experiments and under the application of high–rate gas injection and withdrawal.

The laboratory experiments performed by *Bannach et al,* [38] will be used as the basis for our validation. The laboratory model is made of stainless steel high–pressure cylindrical vessel (Fig. B.1), with dimensions: height ($L = 1.0$ m), and radius ($R = 0.18$ m). The model is equipped with an overall heating system to allow for simulation of buoyant forces as result of geothermal gradients.

We will be attempting to reproduce the experimental results of two test sequences: 1) test 7 for investigating pressure and temperature development during gas injection; and, 2) test 14 for investigating pressure and temperature development during gas withdrawal. Nitrogen was used as the test fluid, the test data for the applied initial and boundary conditions is presented in Table (B.1).

Tests were performed by establishing the desired initial and boundary conditions (in terms of pressure and temperature). Figure (B.2) shows the injection and withdrawal rates as implemented by *Bannach et al,* [38] for tests 7 and 14. Same rate schemes were fed to COMSOL in order to compare simulations to experimental data.

The Beattie–Bridgeman model is used to describe the thermodynamic behavior of nitrogen as a real gas [39]. This model is based on five experimentally determined constants, it is expressed as,

$$p = \frac{R\,T}{(M_w\,\nu)^2}\left(1 - \frac{c}{M_w\,\nu\,T^3}\right)\Big(M_w\,\nu + B\Big) - \frac{A}{(M_w\,\nu)^2}, \tag{B.1}$$

with $A = A_0\Big[1 - a/(M_w\,\nu)\Big]$ and $B = B_0\Big[1 - b/(M_w\,\nu)\Big]$, M_w is the nitrogen molecular weight. The equation is known to be reasonably accurate for densities up to $0.8\rho_{\rm cr}$, where $\rho_{\rm cr}$ is the density of the substance at its critical point. Table (B.2) shows the the values of the constants needed to predict the real gas thermodynamic behavior of nitrogen.

COMSOL provides the temperature evolution functions of nitrogen specific heat C_p, dynamic viscosity μ, and thermal conductivity Λ. The experimental data shows a maximum temperature change of [10 to

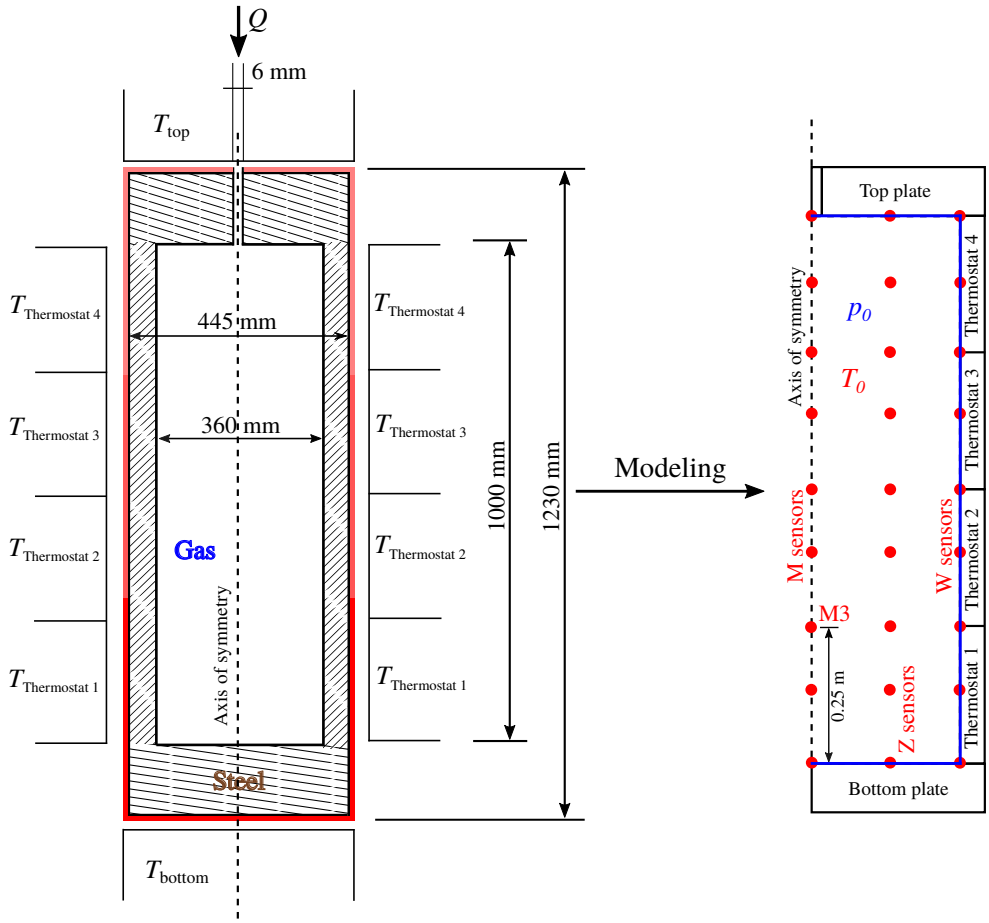

Figure B.1: Schematic diagram of the laboratory model used to validate the turbulent thermodynamic flow of gas in underground caverns. The figure shows the axes where the vertical temperature profiles are to be measured, ten sensors over each vertical axis: sensors M (central), Z (at $r = R/2$), and W (by the wall). Sensor M3 is displayed exclusively as experimental temperature profile histories will be compared to simulation results at this location.

65] °C in the two tests of injection and withdrawal. For this temperature range, nitrogen thermodynamic properties take the following values: $C_p \in [1039.5 - 1040.5]$ J/kg/K, $\mu \in [1.7 - 1.92] \times 10^{-5}$ Pa s, and $\Lambda \in [0.025 - 0.0285]$ W/m/K. Steel thermal diffusivity was set equal to $\kappa_s = 1.25 \times 10^{-5}$ m^2/s.

Appendix B.1. The numerical model

The temperature boundary conditions and initial values $T(0)$ and $p(0)$ presented in Table (B.1) were applied to the model shown in Fig. B.1. The injection and withdrawal rates (Fig. B.2) where set to the inlet and gas was injected at the room temperature ($T = 12$ °C).

Only half of the domain was simulated due to axial symmetry (Fig. B.3). The geometry was discretized into 102984 elements that included 5052 quadrilateral boundary elements and 1739 edge elements. The domain is excessively refined near the boundaries. This refinement is meant to recover the effect of

Table B.1: Test specifications as performed by *Bannach et al*, [38]: Tests 7 and 14

		Test 7 (Injection)	Test 14 (Withdrawal)
Pressure	Start	60.7 bar	100.3 bar
	End	94.4 bar	1.1bar
Average temperature	Start	48.9 °C	48.7 °C
	End	48.9 °C	48.9 °C
Boundary temperature	Top plate	46.0 °C	46.0 °C
	Thermostat 4	46.0 °C	46.0 °C
	Thermostat 3	48.0 °C	48.0 °C
	Thermostat 2	50.0 °C	50.0 °C
	Thermostat 1	53.5 °C	53.5 °C
	Bottom plate	53.5 °C	53.5 °C
Duration of treatment	(injection/withdrawal)	170 s	∼500 s

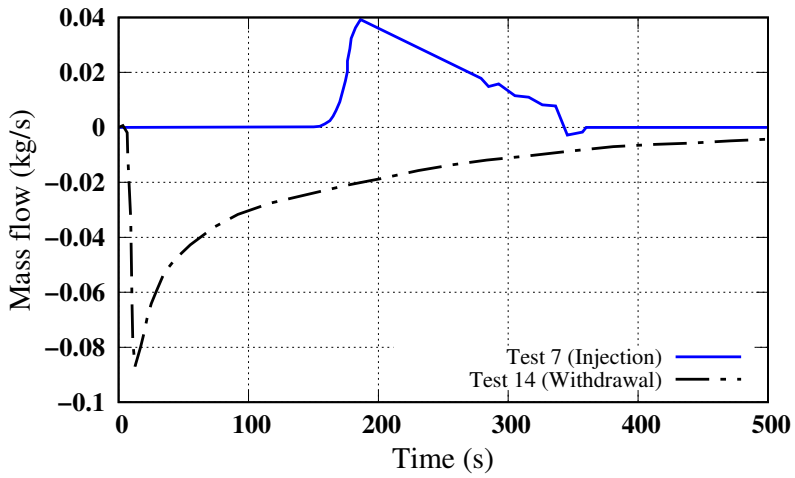

Figure B.2: Mass flow rates implemented in tests 7 and 14. The graph data was digitized from *Bannach et al,* [38].

Table B.2: Beattie–Bridgeman model constants for nitrogen as described in Eq. B.1.

A_0	a	B_0	b	c
136.2315	0.02617	0.05046	-0.00691	4.20×10^4
$T_{cr} = 126.20$ (K), $p_{cr} = 3398.441$ (kPa), and $\rho_{cr} = 311.22$ (kg/m^3)				

374 convective heat transfer due to the gas speeding by the model wall.

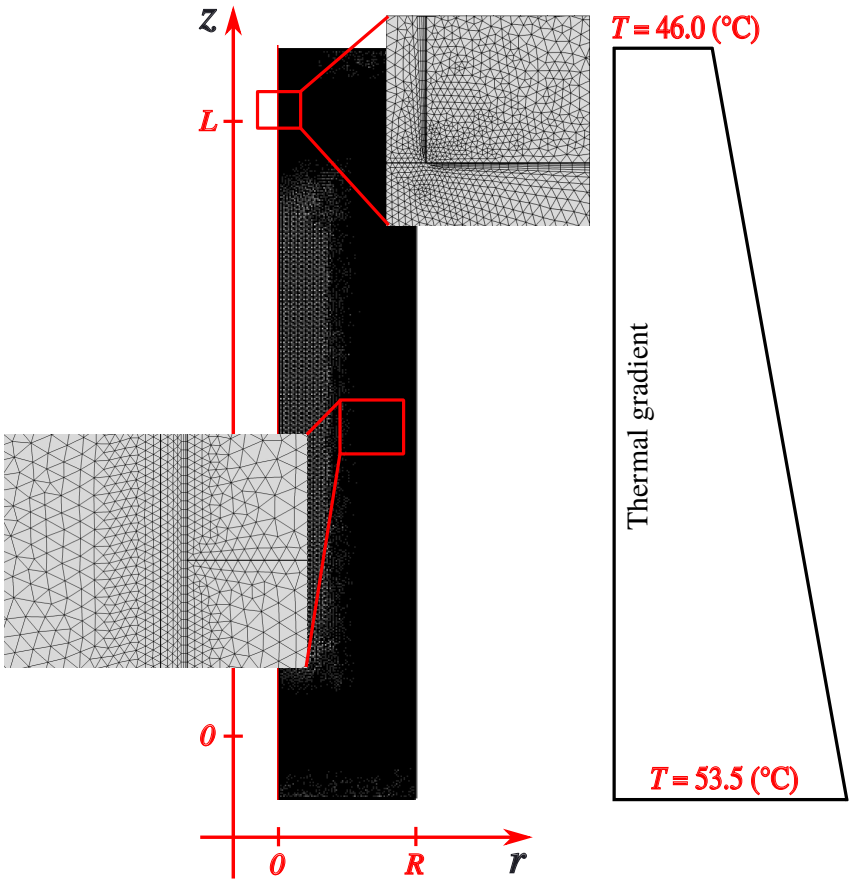

Figure B.3: Discretization of the numerical model to simulate tests 7 and 14 [38]. Temperature boundary conditions and initial values $T(0)$ and $p(0)$ were set up as mentioned in Table (B.2), gas was then injected or withdrawn following the program of Fig. B.2. The mesh contains 102984 elements of which 5052 quadrilateral boundary elements.

Appendix B.2. Simulation results of test 7 (Injection)

Figure B.4(a) shows the development of the temperature profiles at sensor M3 along the model central axis at location ($r = 0$, $z = L/4$). Sensor M3 was chosen since most of the turbulent effects happen at the bottom of the model. Consequently, most of the discrepancies between simulations and laboratory measurements are expected to take place in that region. The figure compares between the numerical responses of laminar and turbulent flows and the experimental data as shown by *Bannach et al*, [38].

There is a good match between the numerical results of turbulent flow and the experimental data. The simulation results for laminar flow are underestimating the true thermodynamic behavior, besides, they show numerical instabilities in–spite of the use of a heavily refined mesh (time–volume averaged Pe = 0.7). The necessity to integrate a turbulent flow model can be conceived from calculating the Reynold's and the Rayleigh numbers. We have averaged these numbers over the model volume and simulation time to get $\mathrm{Re} = 1.72 \times 10^5$ and $\mathrm{Ra} = 6.39 \times 10^{11}$. Both numbers exceed the limits for laminar flow which makes

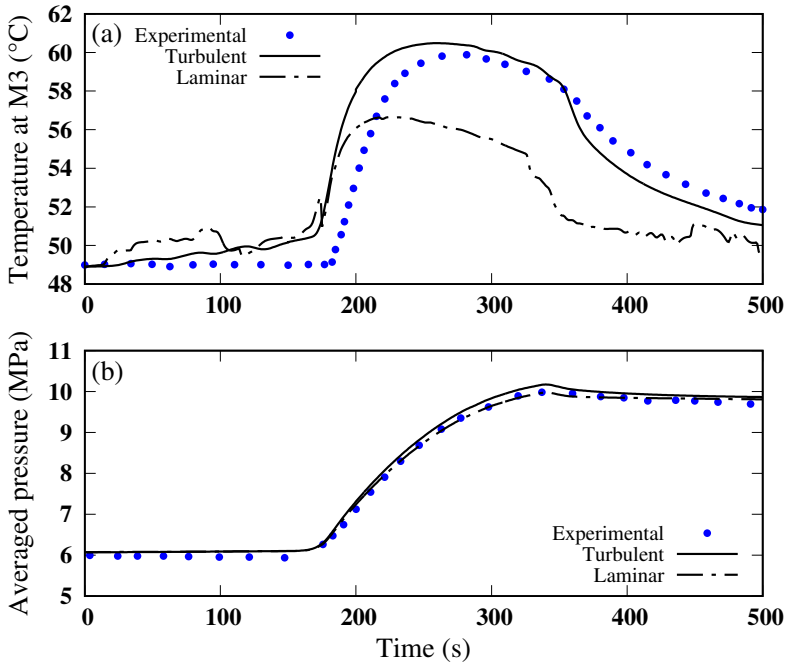

Figure B.4: Injection test 7: a) Comparison between the experimental [38] and the simulated temperature profiles (for laminar and turbulent flows) at sensor M3 along the model central axis at location ($r = 0, z = L/4$). b) Comparison between experimental and simulated volume averaged pressure histories for laminar and turbulent flows.

the use of the k-ϵ model appropriately needed. Since the calculated gas pressure is predominately related to the injected mass, Fig. B.4(b) shows a quite good agreement between experimental and numerical simulations for both laminar and turbulent flows.

Figure B.5(a) shows the history of gas velocity magnitude at sensor M3 and compares the simulation results for the laminar and turbulent flow models. The laminar flow model is overestimating the gas velocity at this point, it also shows numerical noises that render the solution inaccurate. Though the laminar flow solution overestimates the gas velocity at this location, it considerably underestimates it and shows an entirely erroneous flow behavior near the model wall (Fig. B.5(b)).

During injection, gas flows up the model wall, however, as soon as injection terminates the gas shows a natural heat convection behavior where flow, at this location, happens down the model wall (Fig. B.5(b)). The laminar flow solution shows erroneous flow behavior in terms of both direction and magnitude, which renders the calculated convected heat transfer incorrect as well.

Appendix B.3. Simulation results of test 14 (withdrawal)

Figure B.6 compares the experimental temperature, at sensor M3, and the volume averaged pressure profiles during the withdrawal test to the numerical simulations for the turbulent flow model.

Figure B.7 compares simulated vertical profiles of the gas temperature along the vertical axes of

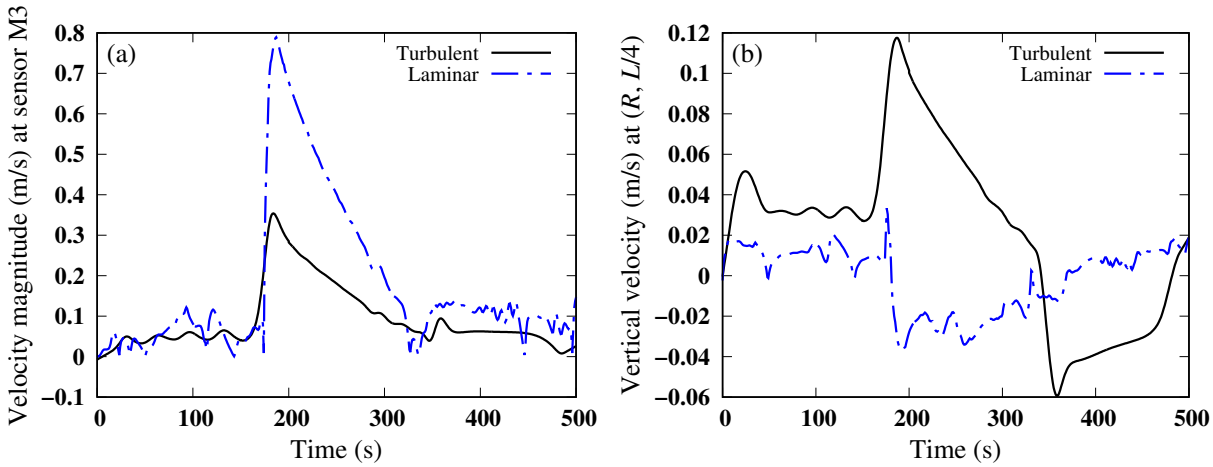

Figure B.5: Injection test 7: a) Gas velocity magnitude history at sensor M3. b) Gas vertical velocity component history at the model wall at location ($r = R$, $z = L/4$). The figure compares between the simulation results of laminar and turbulent flow models.

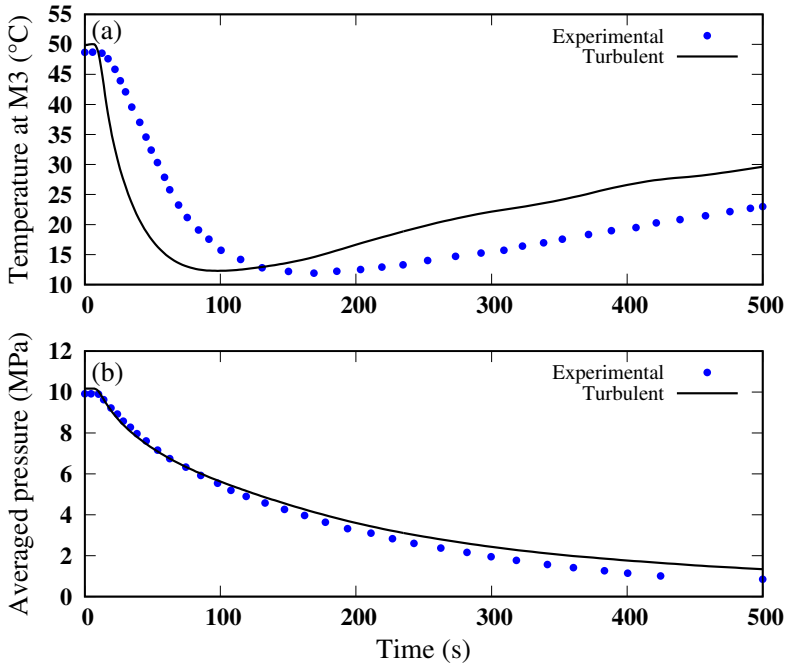

Figure B.6: Withdrawal test 14: a) Comparison between the experimental [38] and the simulated temperature profiles at sensor M3 along the model central axis at location ($r = 0$, $z = L/4$). b) Comparison between experimental and simulated volume averaged pressure histories.

distances $r = 0$ (model central axis, M sensors), $r = R/2$ (Z sensors), and $r = R$ (model wall, W sensors) to the experimental measurements. This type of validation was only shown for test 14 as we did not have the same kind of measurements for the injection test 7.

In general there is a good agreement between the experimental measurements and the numerical

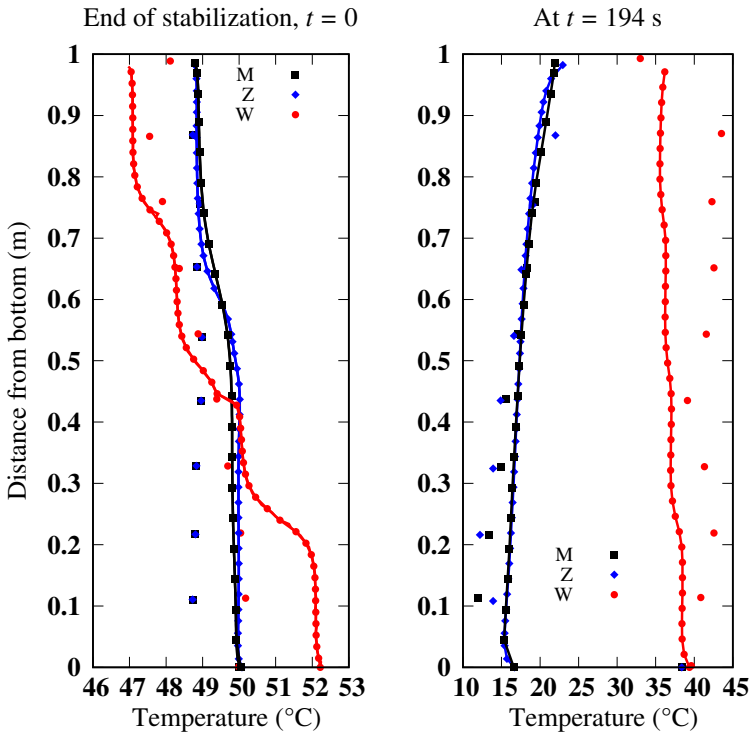

Figure B.7: Developed temperature profiles along the model height during the withdrawal test 14: comparison between the experimental record (marked data), and our simulations (solid marked lines). M sensors are placed at the centre line of the model ($r = 0$), Z sensors are placed at distance ($r = R/2$) from the centre line, and W sensors are placed at the model walls ($r = R$).

simulations with a turbulent flow model. Discrepancies can be related to several factors, of which the fact that *Bannach et al,* [38] performed their tests while having a bowl of brine inside the model, i.e. certain degree of vapor presence.

Figure B.8 shows gas velocity contours and flow patterns during injection at $t = 320$ s and withdrawal at $t = 194$ s. Though the gas velocity in the withdrawal tube is almost seventh fold the value during the injection test, only small model volume near the tube is affected and the gas average velocity magnitude remains in the range shown in the graph, i.e. 0.02 to 0.14 m/s. However, in case of injection, a large model volume is affected by the high tube velocity, as can be shown in the dark red region excluded from the velocity magnitude range. The differences in the calculated tube velocity are attributed to the assigned mass rates. Following Fig. B.2, at time $t = 320$ s, the injected mass rate is $Q \simeq 0.01$ kg/s, meanwhile $Q \simeq -0.02$ kg/s during withdrawal at $t = 194$ s.

It is also observed that, even at this low rate of injection ($t = 320$ s and $Q = 0.007$ kg/s), gas hits the bottom of the model. We do not expect this to happen in the real caverns where we anticipate gas velocity to almost vanish before crossing half the model height (at least in case of seasonal cycling).

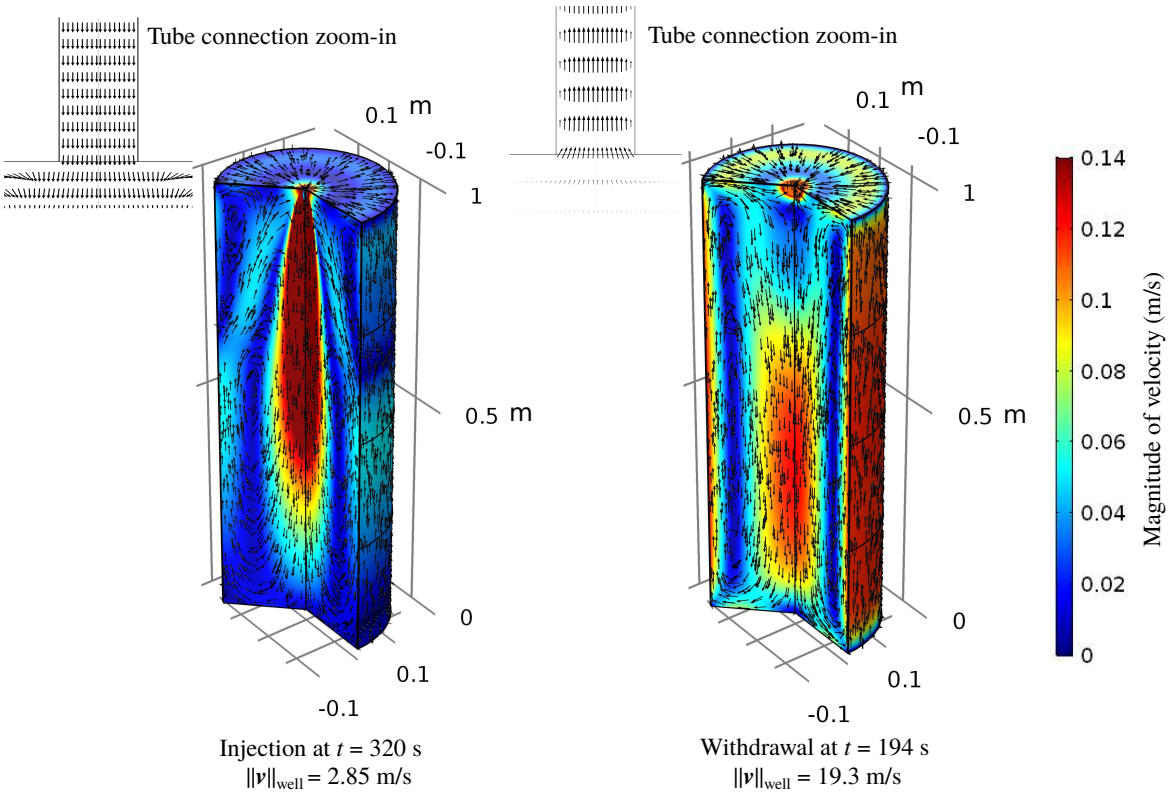

Figure B.8: Gas velocity contours during test 7 (injection) at $t = 320$ s, and during test 14 (withdrawal) at $t = 194$ s. The figure also shows a 2–D zoom–in at the tube connection to show the flow in/out the model volume. The tube gas velocity ($||\boldsymbol{v}||_{\text{well}}$) is also displayed at the same time.

Appendix B.4. Choice of mesh

CFD simulations require the generated mesh to have high quality, enough resolution for the desired accuracy, and to be computationally at a low cost. Usually such meshes need to be excessively refined in regions of sharp gradients for the three fields of unknowns. Therefore, our mesh was heavily refined near the model wall, along the injection well, and near the entrance where gas goes into the model volume.

Our numerical solution stopped to be mesh dependent at meshes contained approximately 70,000 elements. However, considering that the simulation time was relatively short, and that we tried to correlate our simulations to experimental data, we chose our mesh so that the volume averaged Péclet number was Pe=0.7. Our objective was to decrease the solution dependency on the stabilization techniques that tend to be diffusive and that may affect the numerical solution for the validation goal of this section.

The evolution of the wall function δ_w^+ (Eq. A.10) during tests 7 and 14 did not exceed 11.062 Pa s, it is around the suggested value (11.06) for good accuracy of the k-ϵ turbulent model [27, 36].

References

[1] Nadau L., Leplay P., Fourmigué J–F., Memponteil A., and Hadj Hassen F. (2015). A regenerator pilot to evaluate the technical and economic relevance of energy storage by adiabatic compressed air energy storage by ceramic media. *In*: The ninth International Renewable Energy Storage Conference, March 2015, Dusseldorf, Germany.

[2] Kushnir R., Dayan A., and Ullmann A. (2012). Temperature and pressure variations within compressed air energy storage caverns. International Journal of Heat and Mass Transfer, 55: 5616–5630.

[3] Götz M., Lefebvre J., Mörs F., Koch A. M., Graf F., Bajohr S., Reimert R., and Kolb T. (2016). Renewable Power-to-Gas: A technological and economic review. Renewable Energy, 85: 1371–1390.

[4] Lehner M., Tichler R., Steinmüller H., and Koppe M. (2014). Power–to–gas: technology and business models. Springer.

[5] Charnavel Y., Leca D., and Poulain F. (1983). Advanced geometrical modelling of salt dissolution during cavern leaching – illustration with a case study. *In*: The SMRI Meeting, Las Vegas, Nevada, USA.

[6] Pernette E. and Dussaud M. (1983). Underground storages at Tersanne and Etrez: prediction and simulation of cavity leaching in a salt layer charged with insoluble materials. *In*: The sixth International Symposium on Salt, Toronto, Canada.

[7] Labaune P. and Rouabhi A. (2019). Dilatancy and tensile criteria for salt cavern design in the context of cyclic loading for energy storage. Journal of Natural Gas Science and Engineering, 62: 314–329.

[8] Böttcher N., Görke U. J., Kolditz O., and Nagel T. (2017). Thermo–mechanical investigation of salt caverns for short–term hydrogen storage. Environmental Earth Sciences, 76: 98.

[9] Guo C., Zhang K., Lehua P., Cai Z., Li C., and Li Y. (2017). Numerical investigation of a joint approach to thermal energy storage and compressed air energy storage in aquifers. Applied Energy, 203: 948–958.

[10] He W., Luo X., Evans D., Busby J., Garvey S., Parkes D., and Wang J. (2017). Exergy storage of compressed air in cavern and cavern volume estimation of the large–scale compressed air energy storage system. Applied Energy, 208: 745–757.

[11] Xia C., Zhou Y., Zhou S., Zhang P., and Wang F. (2015). A simplified and unified analytical solution for temperature and pressure variations in compressed air energy storage cavern. Renew Energy, 74:718–726.

[12] Serbin K., Ślizowski J, Urbańczyk K., and Nagy S. (2015). The influence of thermodynamic effects on gas storage cavern convergence. International Journal of Rock Mechanics and Mining Sciences, 79:166–171.

[13] Rutqvist J., Kim H–M., Ryu D–W., Synn J–H., and Song W–K. (2012). Modeling of coupled thermodynamic and geomechanical performance of underground compressed air energy storage in lined rock caverns. International Journal of Rock Mechanics and Mining Sciences, 52: 71–81.

[14] Raju M. and Khaitan K. S. (2012). Modeling and simulation of compressed air storage in caverns: A case study of the Huntorf plant. Applied Energy, 89: 474–481.

[15] Barajas P. and Civan F. (2014). Effective modeling and analysis of salt–cavern natural–gas storage. Society of Petroleum Engineers, SPE 164489 at the SPE Production and Operations Symposium, Oklahoma City, Oklahoma, USA, 23–26 March 2013.

[16] Tietze V. and Stolten D. (2015). Comparison of hydrogen and methane storage by means of a thermodynamic analysis. International Journal of Hydrogen Energy, 40(35):11530–11537.

[17] Spiegel E. A and Veronis G. (1960). On the Boussinesq approximation for a compressible fluid. Astrophysical Journal, 131: 442–447.

[18] Edwards P. P., Kuznetsov V. L., David W. I. F., and Brandon N. P. (2008). Hydrogen and fuel cells: Towards a sustainable energy future. Energy Policy, 36: 4356–4362.

[19] Rouabhi A., Hévin G., Soubeyran A., Labaune P., and Louvet F. (2017). A multiphase multicomponent modeling approach of underground salt cavern storage. Geomechanics for Energy and the Environment, 12: 21–35.

[20] Labaune P., Rouabhi A., Tijani M., Martin L. B., You T. (2018). Dilatancy criteria for salt cavern design: a comparison between stress– and strain–based approaches. Rock Mechanics and Rock Engineering, 51(2): 599–611.

[21] Bormann A. S. (2001). The one–set of convection in the Rayleigh–Bénard problem for compressible fluids. Continuum Mechanics and Thermodynamics, 13(1): 9–23.

[22] Sankar M., Park Y., Lopez J. M., and Do Y. (2011). Numerical study of natural convection in a vertical porous annulus with discrete heating. International Journal of Heat and Mass Transfer, 54: 1493–1505.

[23] Loret B. (2018). Fluid injection in deformable geological formations: Energy related issues. Springer International Publishing AG, Gewerbestrasse 11, 6330 Cham, Switzerland.

[24] Sun X., Ye Z., Li J., Wen K., and Tian H. (2019). Forced convection heat transfer from a circular cylinder with a flexible fin. International Journal of Heat and Mass Transfer, 128: 319–334.

[25] Karimi–Jafari M. (2010). Comportement transitoire des cavités salines profondes, PhD thesis (French), Science de l'Ingénieur [Physics], Ecole Polytechnique X, Paris, France.

[26] Wilcox C. D. (2016). Turbulence modeling for CFD. DCW industries, Inc, 5354 Palm Drive, La Cañada, California 91011, USA.

[27] Kuzmin D., Mierka O., and Turek S. (2007). On the implementation of the k-ϵ turbulence model in incompressible flow solvers based on a finite element discretization. International Journal of Computing Science and Mathematics, 1(2–4): 193–206

[28] Lew A. J., Buscaglia G. C., and Carrica P. M. (2001). A note on the numerical treatment of the k-ϵ turbulence Model. International Journal of Computational Fluid Dynamics, 14: 201–209.

[29] Wright N. G. and Easom G. J. (2003). Non–linear k-ϵ turbulence model results for flow over a building at full-scale. Applied Mathematical Modelling, 27: 1013–1033.

[30] Braga J. E. and de Lemos J. S. M. (2008). Computation of turbulent free convection in left and right tilted porous enclosures using a macroscopic k-ϵ model. International Journal of Heat and Mass Transfer, 51: 5279–5287.

[31] AbuAisha M. and Loret B. (2016). Stabilization of forced heat convections: Applications to Enhanced Geothermal Systems (EGS). Transport in porous Media, 112: 229–252.

[32] Braga J. E. and de Lemos J. S. M. (2009). Laminar and turbulent free convection in a composite enclosure. International Journal of Heat and Mass Transfer, 52: 588–596.

[33] Kakaç S. and Yener Y. (1995). Convective heat transfer. Second edition, CRC Press, Florida, USA.

[34] Kaviany M. (2002). Principles of heat transfer. John Wiley & sons. New York, USA.

[35] Xu B., Li P. W., and Chan C. L. (2012). Extending the validity of lumped capacitance method for large Biot number in thermal storage application. Solar Energy, 86: 1709–1724.

[36] Lacasse D., Turgeon E., and Pelletier D. (2004). On the judicious use of the k-ϵ model, wall functions and adaptivity. International Journal of Thermal Sciences, 43: 925–938.

[37] Blocken B., Stathopoulos T., and Carmeliet J. (2007). CFD simulation of the atmospheric boundary layer: wall function problems. Atmospheric Environment, 41: 238–252.

[38] Bannach A., Wagler T., Walden S., and Klafki M. (2005). Technology enhancement for 1) inventory assessment and mechanical integrity testing of gas–filled solution mined caverns and 2) mechanical integrity tests of solution mines and liquid storage caverns. GRI–05/0175 project final report, prepared for Gas Research Institute (contract number 8750), D–095596 Freiberg, Germany.

[39] Deming W. E. and Shupe E. L. (1930). The constants of the Beattie–Bridgeman equation of state with Bartlett's P–V–T data on nitrogen. Journal of the American Chemical Society, 52(4): 1382–1389.